Sánchez-Tovar, R.; Blasco-Tamarit, E.; Ibáñez-Arlandis, L.; Fernández Domene, RM.; Roselló-Márquez, G.; Garcia-Anton, J. (2021). Novel TiO2-WO3 self-ordered nanotubes used as photoanodes: Influence of Na2WO4 and H2O2 concentration during electrodeposition. Surface and Coatings Technology. 415:1-13. https://doi.org/10.1016/j.surfcoat.2021.127124

# Novel $TiO_2$-$WO_3$ self-ordered nanotubes used as photoanodes: influence of $Na_2WO_4$ and $H_2O_2$ concentration during electrodeposition

**Sánchez-Tovar, R. [a]; Ibañez-Arlandis, L. [b]; Blasco-Tamarit, E. [b]; Fernández-Domene, R.M. [a]; Roselló-Márquez, G. [b]; García-Antón, J.[b]**

[a]*Departmento de Ingeniería Química, Universitat de València, Av de les Universitats, s/n, 46100 Burjassot, Spain*

[b] *Ingeniería Electroquímica y Corrosión (IEC), Instituto Universitario de Seguridad Industrial, Radiofísica y Medioambiental (ISIRYM), Universitat Politècnica de València, Camino de Vera s/n, 46022 Valencia, Spain.* *jgarciaa@iqn.upv.es* (J. García-Antón), rita.sanchez@uv.es (R. Sánchez-Tovar)

## ABSTRACT

Hybrid $TiO_2$-$WO_3$ nanostructures has been synthesized by electrochemical anodization under controlled hydrodynamic conditions followed by electrodeposition in the presence of different contents of $Na_2WO_4$ (5, 15 and 25 mM) and $H_2O_2$ (20, 30 and 40 mM). The influence of the electrolyte used for electrodeposition on the morphology, crystalline structure and photoelectrochemical response for water splitting has been evaluated through Field Emission Electronic Microscopy, High-Resolution Transmission Electron Microscopy, Confocal Raman Spectroscopy, Grazing Incidence X Ray Diffraction, X-Ray Photoelectron Spectroscopy, Atomic Force microscopy and photocurrent versus potential measurements. Additionally, a statistical multi-factor categorical analysis was performed to determine the most significant influential parameters. Results show that hybrid $TiO_2$-$WO_3$ nanostructures formed by simple anodization and subsequent electrodeposition with 30 mM $H_2O_2$ and 25 mM $Na_2WO_4$ present the highest photocurrent response, 60 % higher if compared to $TiO_2$ anodized nanotubes, solving the main

problems presented during the usual fabrication of heterostructures, i.e. high temperatures, pressures, number of chemicals and time.

**Keywords:** $TiO_2$-$WO_3$ nanostructures, anodization, electrodeposition, photoelectrocatalysis, water splitting

## 1. INTRODUCTION

Global energy demand, mainly based on finite resources, has grown considerably during the last decades. This implies, on the one hand, the near depletion of these resources and, on the other hand, a significant environmental contamination [1, 2]. For this reason, there is a need for developing new environmental friendly sources of energy which also guarantee global energy consumption, as well as promote the use of renewable energies, such as hydraulic, solar and wind energy [1, 3].

Currently, the use of hydrogen as an energy vector has become one of the most promising options to mitigate the negative impact produced on the environment by fossil fuels, such as climate change and air pollution [1]. The main advantage of hydrogen is that it could be generated by means of renewable energy sources and water without the emission of any type of pollutant to the environment [4]. In addition it possesses a high capacity for energy storage, with an energy content per unit weight of 120 kJ/g [4, 5].

One of the most promising and novel methods for hydrogen production is photoelectrocatalysis by using sunlight [6]. In this process, water molecules are divided into hydrogen and oxygen by applying direct electrical current [6, 7]. The small amount of energy that is needed can be provided by renewable energy sources [8]. To carry out the photoelectrochemical reaction it is required the use of a semiconductor electrode that

absorbs sunlight. This work proposes hybrid $TiO_2$-$WO_3$ nanostructures as photoanodes to increase the efficiency of the process.

Titanium dioxide ($TiO_2$) is the most encouraging and widely studied photoanode [9] due to its excellent properties, such as resistance to corrosion and photocorrosion [10], high photochemical stability in acid and basic environments [11], its zero toxicity [12] and low cost [13]. In addition, $TiO_2$ has a band-gap position appropriate for water splitting [14] and for the elimination of organic pollutants [12].

In the last decades, various types of $TiO_2$ nanostructures have been developed for photoelectrochemical applications in order to maximize the specific surface area of the photoanode [14]. One of the most promising structure is the $TiO_2$ nanotubes, which present a unidirectional path to the flow of electrons and reduce possible recombination between the electron-hole pairs. Furthermore, they have a higher specific surface area compared to other developed structures [15].

These $TiO_2$ nanotubes can be developed from several techniques, nevertheless the electrochemical anodization, especially, when it is performed under hydrodynamic flow conditions is a relatively recent and novel one. This technique allows controlling the dimensions of the nanotubes by changing their characteristic parameters such as electrode rotation speed, potential and so on [12, 14]. Likewise, the $TiO_2$ nanotubes are formed directly on the metallic titanium substrate and have good adhesion resistance [16].

However, titanium dioxide has the disadvantage of possessing a low overall yield [17] due to its wide band-gap (3.2 eV for anatase and 3.0 eV for rutile) that only allows the absorption of light in the UV range with wavelength smaller than 380nm [18], which represents less than 5% of the solar radiation [19-21].

Tungsten trioxide ($WO_3$), like $TiO_2$, is an n-type semiconductor widely studied for various photocatalytic applications, such as the photoelectrochemical water splitting [9] and the degradation of pollutants [22]. This semiconductor has various favourable properties for photocatalysis, that is the absorption of visible light, high resistance to photocorrosion and its charge-carrying capacity [23]. Furthermore, it exhibits a band-gap value of roughly 2.6 eV, which indicates an absorption of approximately 12% of the solar spectrum [9] and also an absorption of the visible spectrum of up to 500 nm [24].

To solve the main drawbacks presented by the pure $TiO_2$ nanostructures, i.e. to narrow the band gap of $TiO_2$ and modify its energy levels, this study proposes the synthesis of hybrid $TiO_2$-$WO_3$ nanostructures as photocatalyst. Since they have adequate physicochemical properties such as resistance to photocorrosion [18] and better stability and photocurrent efficiency compared to pure $TiO_2$ and $WO_3$ nanostructures [25, 26]. $W^{+6}$ possesses an ionic radius close to the $Ti^{+4}$, in this way, $WO_3$ might couple into the $TiO_2$ during annealing [21, 27]. The incorporation of $WO_3$ to $TiO_2$ will contribute to reduce the band gap value of $TiO_2$ [28, 29]. This is an important advantage for photoelectrolytic water splitting since it allows the process to be carried out using visible light [30, 31]. In addition, its valence and conduction bands are lower than the ones obtained for $TiO_2$, thus avoiding charge recombination [32].

Until the present, various techniques have been proposed to synthetize hybrid $TiO_2$-$WO_3$ nanostructures, such as sol-gel method, hydrothermal, anodization, wet impregnation, radiofrequency spraying, etc. [33]. In this study the fabrication of hybrid nanostructures will be carried out by electrochemical anodization of $TiO_2$ and subsequent $WO_3$ electrodeposition.

The electrodeposition technique is one of the most promising techniques for the incorporation of $WO_3$ into $TiO_2$ nanostructures, as well as one of the most economical.

This method is based on the cathodic reduction of a peroxide precursor, which is obtained by the interaction of tungsten with hydrogen peroxide ($H_2O_2$) [34]. The precursor is described as a dimer with the formula of $W_2O_{11}^{2-}$ with a peroxo ligand ($O_2^{2-}$), leaving the tungsten with an oxidation state +6 [34, 35].

Some studies [36, 37] have developed structures of $TiO_2$-$WO_3$ adding $WO_3$ by electrodeposition, which differ from each other in the concentration of $Na_2WO_4$ and $H_2O_2$ in the electrolyte. The present study adds the novelty of synthesizing $TiO_2$ nanotubes under hydrodynamic flow conditions by electrochemical anodization, and then performs an electrodeposition to form the hybrid nanostructure, varying the concentrations of $Na_2WO_4$ and $H_2O_2$ in the electrolyte, to optimize and evaluate the most significant parameters of the photoelectrochemical water splitting. This novel combination of both methods could solve most of the problems presented by some of the techniques found in literature, such as the high temperature in the sol-gel method [38-40], the low pressures required in radiofrequency spraying [15] and the long time required for the hydrothermal process [39].

## 2. EXPERIMENTAL PROCEDURE

### *2.1. Hybrid nanostructure synthesis*

To form the hybrid nanostructures a two-step method was followed, i.e.; first electrochemical anodization was carried out to create the $TiO_2$ nanotubes, and then $WO_3$ was electrodeposited on the $TiO_2$.

First of all, titanium rods (8 mm in diameter) were subjected to a surface treatment, which consisted of abrading the surface of the sample with sandpaper type SiC of different granulometry (220, 500 and 4000). Then, the titanium rod was cleaned in ethanol in an

ultrasonic bath for 2 min, rinsed with deionized water and dried with nitrogen. Finally, for the electrochemical anodization, the titanium rod was coated with teflon (to expose an area of 0.5$cm^2$ to the electrolyte) and immersed in the anodization electrolyte. For anodization, titanium rods served as the working electrode (anode) and a platinum foil (1 $cm^2$) was used as the cathode. A potential difference between anode and cathode of 55 V was applied during 30 min and the titanium rod was connected to a rotating disk electrode (RDE) to establish hydrodynamic conditions of 3000 rpm during anodization. The electrolyte used for anodization consisted of an ethylene glycol based (EG) with 1 M of water and 0.05 M of ammonium fluoride ($NH_4F$).

Once the sample was anodized, tungsten trioxide ($WO_3$) was electrodeposited on the formed $TiO_2$ nanotubes, in a three-electrode electrochemical cell. A platinum foil was the counter electrode, a silver/silver chloride (Ag/AgCl, 3M KCl) the reference electrode and the $TiO_2$ samples the working electrode. In order to optimize the electrodeposition process, different concentrations of $Na_2WO_4$ (5, 15, 25 mM) and $H_2O_2$ (20, 30, 40 mM) were used. The applied potential was fixed at -0.44$V_{Ag/AgCl}$ for 150 seconds.

After electrodeposition, the hybrid nanostructures were annealed in an oven to transform the amorphous structure into a crystalline one. The annealing treatment was carried out for 2h at 450°C, using a heating rate of 30 °C/min.

*2.2. Characterization of the nanostructures*

To evaluate the crystalline structure of the samples a Confocal Raman Microscope with a wavelength (λ) of 488mn (blue laser) was used. Grazing Incidence X Ray Diffractometer measurements (GIXRD) were performed with a Bruker D8AVANCE diffractometer with Cu radiation operating at 30 mA and 40 kV from 20º to 60º and a

grazing incidence of 2º. The electronic states of the nucleus and of the valence of the $TiO_2$-$WO_3$ nanostructures were analyzed through X-ray photoelectron spectroscopy (XPS, K-ALPHA, Thermo Scientific). Al-K_radiation (1486.6 eV) monochromatized by a twin crystal monochromator providing a focused X-ray spot at 3 mA × 12 kV was used to collect the spectra. The alpha hemispherical analyzer operated in the constant energy mode by using 200 eV survey scan pass energies. The morphology of the hybrid nanostructures was observed by a Field Emission Scanning Electron Microscope (FE-SEM) with Energy-dispersive X-ray spectroscope (EDX) for identification of elements.

TEM Analysis of the $TiO_2$-$WO_3$ nanostructures was performed by High Resolution Transmission Electron Microscopy (HRTEM) with a field emission gun TECNAI G2 F20 microscope operated at 200 kV, having the capabilities of selected area electron diffraction (SAED) and energy dispersive X-ray spectroscopy (EDX). Samples were analyzed by EDX in TEM microscope and the distribution of Ti and W along the nanotubes was determined by using EDX-mapping in nanoprobe mode. In order to prepare the TEM samples, a piece of the $TiO_2$-$WO_3$ nanostructures was deposited onto a holey-carbon film supported on a copper grid.

In addition, the roughness of the nanostructures was characterized using an Atomic Force Microscope (AFM), by the calculation of the Sa parameter (arithmetical mean height of the surface). The AC mode (an intermittent contact regimen) was used with an oscillating cantilever (0.5 V).

*2.3. Photoelectrochemical response tests*

Photoelectrochemical response of the nanostructures was carried out using the samples as photoanodes with a solar simulator (AM 1.5 conditions at 100 $mW \cdot cm^{-2}$) connected to a potentiostat. The electrochemical cell consisted of three electrodes, using the $TiO_2$-

$WO_3$ photocatalyst as the working electrode (with an area of 0.26 $cm^2$ exposed to the electrolyte), an Ag/AgCl (3M KCl) as the reference electrode, and a platinum foil as the counter electrode, immersed in the electrolyte ($H_2SO_4$ 0.1M aqueous solution). The tests were carried out applying different potential step pulses with and without light (intervals of 60 mV in dark conditions and 20 mV with light), from an initial potential of -0.24$V_{Ag\,/\,AgCl}$ until 1$V_{Ag/AgCl}$.

*2.4. Statistical analysis*

Finally, a multi-factor categorical analysis was performed with the Statgraphics Centurion software in order to determine the most significantly influential parameters. The experimental factors to consider were the concentration of $Na_2WO_4$ (5, 15, 25 mM) and $H_2O_2$ (20, 30, 40 mM), with the photocurrent obtained at 0.7 $V_{Ag/AgCl}$ as the response variable.

## 3. RESULTS AND DISCUSSION

*3.1. Electrochemical hybrid nanostructure formation*

First of all, electrochemical anodization was carried out under hydrodynamic flow conditions to fabricate the $TiO_2$ nanotubes. Fig. 1 shows three different stages during anodization when the current density is registered as a function of time.

In the first stage (I), the current density markedly decreases until it reaches a minimum value. This corresponds to the formation of a $TiO_2$ layer that opposes a resistance to the pass of electric current as the layer is being formed and therefore, current density decreases. During this stage, the oxidation of metallic titanium to $Ti^{+4}$ occurs at the anode

(Eq.1) and this ion reacts with water in the medium to form an oxide layer ($TiO_2$) on the surface of the metallic titanium according to the Eq.2 [16].

$$Ti \rightarrow Ti^{+4} + 4e^{-} \quad \text{Eq.1}$$

$$Ti^{+4} + 2H_2O \rightarrow TiO_2 + 4H^{+} \quad \text{Eq.2}$$

In the second stage (II), the presence of fluorides in the medium begins to dissolve the formed oxide layer, thus increasing the current density until it reaches its maximum value. This is due to the formation of titanium hexafluoride $[TiF_6]^{-2}$. This complex can be formed by the union of fluoride ions ($F^-$) and $Ti^{+4}$ ions generated at the electrode-electrolyte interface according to Eq.3 [12]; and by the slow but continuous dissolution of the deposited $TiO_2$, according to Eq.4 [41].

$$Ti^{+4} + 6F^{-} \rightarrow [TiF_6]^{-2} \quad \text{Eq.3}$$

$$TiO_2 + 4H^{+} + 6F^{-} \rightarrow [TiF_6]^{-2} + 2H_2O \quad \text{Eq.4}$$

Finally, in stage III the current density remains practically constant until the end of the test, which indicates the gradual formation of the nanotubes. In addition, a balance between the formation and dissolution of the $TiO_2$ occurs.

Once the $TiO_2$ nanotubes are formed, the $WO_3$ is added. This process is based on the cathodic reduction of a peroxide precursor ($W_2O_{11}^{2-}$ = $[(O)W(O_2)_2(O)(O_2)_2W(O)]^{2-}$) formed by mixing hydrogen peroxide ($H_2O_2$) with sodium tungstate ($Na_2WO_4$) according to Eq.5. During the process, the transport of electrons occurs at the electrode/electrolyte interface due to the presence of protons ($H^+$) and $H_2O_2$ in the electrolyte, and the $[W_2O_{11}]^{-2}$ will be gradually dissociated to tungsten trioxide (Eq.6), which will be deposited on the previously formed $TiO_2$ nanotubes [42, 43]. Eq. 6 takes place since the peroxo (with valence number equal to -1) of the precursor reduces to oxygen present in

the $WO_3$ (with valence number -2) and oxidizes to oxygen gas (with valence number 0). Thus, forming the hybrid $TiO_2$-$WO_3$ nanostructure.

$$2H^+ + 2WO_4^{2-} + 4H_2O_2 \rightarrow W_2O_{11}^{-2} + 5H_2O \quad \text{Eq.5}$$

$$W_2O_{11}^{2-} + (2+x)H^+ + xe^- \rightarrow 2WO_3 + (2+x)/2H_2O + (8-x)/4O_2 \quad \text{Eq.6}$$

According to Eq. 5 and 6, both the presence of higher amounts of $Na_2WO_4$ and $H_2O_2$ should produce more $[W_2O_{11}]^{-2}$ complex and, consequently, more $WO_3$. However, higher $H_2O_2$ contents might cause the dissociation of $WO_3$ back to the intermediate compound $[W_2O_{11}]^{-2}$ as indicated by Eq.7 [43].

$$2WO_3 + 4H_2O_2 \rightarrow W_2O_{11}^{-2} + 2H^+ + 3H_2O \quad \text{Eq.7}$$

*3.2. Confocal Raman Microscopy and GIXRD measurements*

In order to obtain information of the crystalline structure of the hybrid nanostructures, a confocal Raman Microscope was used with a wavelength of 488 nm (blue laser).

Figure 2 shows the peaks of the Raman spectrum corresponding to the characteristic spectrum of $TiO_2$ in its anatase phase (156.1, 399.8, 521.7 and 643.5 $cm^{-1}$) [30], confirming the transformation of amorphous $TiO_2$ to its anatase phase after the heat treatment.

Subsequently, in Figure 2, the different spectra obtained at a constant concentration of $H_2O_2$ and varying the amount of electrodeposited $WO_3$ is analyzed. In relation to this, a slightly more pronounced peak in the spectra at approximately 800 $cm^{-1}$ is observed. Several studies relate this Raman shift with the characteristic peak of monoclinic $WO_3$ [30, 43].

In the samples synthesized with $Na_2WO_4$ concentrations of 25 mM, the characteristic peak of $WO_3$ is clearly observed, whereas for samples electrodeposited at 15 mM $Na_2WO_4$ the peak is less pronounced. The presence of $WO_3$ in the samples was corroborated by means of Raman spectroscopy when performing the electrodeposition with a hydrogen peroxide concentrations of 20 and 30 mM (Fig. 2a) and Fig. 2b)) and a $Na_2WO_4$ concentration of 15 and 25 mM.

Samples electrodeposited at 40 mM $H_2O_2$ (Fig. 2c)) do not clearly show the characteristic $WO_3$ peak for any of the different $Na_2WO_4$ concentrations. This may be owing to the fact that a higher concentration of hydrogen peroxide is able to dissolve part of the $WO_3$ [43]. The same occurs with the samples synthesized with 5 mM $Na_2WO_4$ at different concentrations of $H_2O_2$. This may be due to the fact that the electrodeposited amount of $WO_3$ is small, so it is not possible to detect its presence using the Raman spectroscopy.

It is important to remark that the intensity of the Raman peaks associated with $TiO_2$ anatase decreases as the $Na_2WO_4$ is increased. This might be related to a uniform $WO_3$ electrodeposition on $TiO_2$ surface.

XRD measurements confirm the Confocal Raman Spectra results. In this way, Figure 3 shows the XRD profiles of the $TiO_2$ and $TiO_2$-$WO_3$ nanostructures electrodeposited with 30 mM $H_2O_2$ and different $Na_2WO_4$ concentrations (5, 15 and 25 mM). For all the samples, anatase and titanium diffraction peaks are observed, being the more intense the corresponding to anatase (101) (see Figure 3) [20]. Additionally, crystalline planes of the monoclinic phase of $WO_3$ at $2\theta$ = 23.15°, 23.48°, 24.25°, 33.35° and 34.27°, are associated to the (002), (200), (020), (022) and (202) [34], which confirm the presence of both $TiO_2$ and $WO_3$ in the nanostructures electrodeposited at 15 mM and higher $Na_2WO_4$ contents. XRD did not detect $WO_3$ at $Na_2WO_4$ concentrations of 5 mM, according to Raman measurements.

*3.3. XPS measurements*

X-Ray Photoelectron Spectroscopy (XPS) technique has been used to confirm the $WO_3$ presence in the hybrid nanostructures. Figure 4 shows, as an example, the count spectrum of the $TiO_2$-$WO_3$ sample electrodeposited with 25 mM $Na_2WO_4$ and 30 $H_2O_2$. The nanostructure is basically made up of three elements: oxygen (O), titanium (Ti) and tungsten (W). The presence of the C 1s peak is related to the surface contamination when the sample was exposed to air before the XPS tests.

The detailed XPS spectra corresponding to O 1s, Ti 2p and W 4f are shown in Figure 5. Figure 5a shows the XPS spectra deconvolution for Ti 2p. The peaks observed at 458.52 eV and 464.52 eV correspond to $Ti^{4+}$ $2p_{3/2}$ and $Ti^{4+}$ $2p_{1/2}$ respectively. After deconvolution, the peaks obtained at energy of 457.24 eV and 463.66 eV represent $Ti^{3+}$ $2p_{3/2}$ and $Ti^{3+}$ $2p_{1/2}$. [44, 45].

The Gaussian-Lorentzian fit of the O 1s peak shows (Figure 5b), at energy of 529.68 eV, the lattice oxygen ($L_0$). The peak at this energy is related to the oxygen atoms fully coordinated with $Ti^{4+}$ and $W^{6+}$. The area of the peak obtained at energy of 531.27 eV is related to the oxygen vacancies in the network ($V_0$). Finally, the peak obtained at energy of 532.7 eV is due to the oxygen dissociation from $H_2O$ or $O_2$ that react on the surface [44].

Figure 5c shows the high resolution XPS spectrum corresponding to Ti3p/Wf4 of the $TiO_2$-$WO_3$ sample. The peak recorded at energy around 37.0 eV corresponds to the peak in the 3p region of $Ti3p_{7/2}$. The peaks that appear at 35.80 eV and 37.90 eV are attributed to $W4f_{7/2}$ and $W4f_{5/2}$ respectively. Their doublet splitting of 2.1 eV confirms that $WO_3$ has been formed [46, 47].

*3.4. Atomic Force Microscope (AFM)*

With the AFM technique it was possible to determine the roughness of the samples. In all cases, Sa values were higher (in almost 5 times) in the hybrid nanostructures (Sa = 244.57 nm, as an example, of the hybrid $TiO_2$-$WO_3$ nanostructure synthesized at 25 mM $Na_2WO_4$ and 30 mM $H_2O_2$) than in the $TiO_2$ nanotubes (Sa = 49.50 nm).

This increase in roughness can be beneficial in photocatalytic applications as the surface area of the sample is increased. However, it must be checked that the electrodeposited $WO_3$ particles do not block the mouth of the nanotubes and prevent the absorption of light, since the effect can be detrimental. For this reason, the morphology of the samples was evaluated by Field Emission Scanning Electron Microscopy (FE-SEM).

*3.5. FE-SEM and EDX analysis*

In order to analyze the morphology of the hybrid $TiO_2$-$WO_3$ nanostructures, Field Emission Scanning Electron Microscopy (FE-SEM) was used Fig. 6a) shows an image of a $TiO_2$ nanostructure obtained by electrochemical anodization without electrodeposition. There the presence of a thin initiation layer on the $TiO_2$ nanotubes is observed in some areas, while in other areas this layer has been removed due to hydrodynamic flow conditions during anodization. This corroborates that hydrodynamic flow conditions minimize, at least, in some areas the initiation layer formed on the nanostructure [48].

Fig. 6b) shows a cross section of the $TiO_2$ nanotubes where it can be observed their ordered and vertical arrangement with an average length of 6.6 ± 0.1 μm. This length, together with their ordered vertical arrangement allow a direct path of the incident electrons, thus favouring the absorption of sunlight in photoelectrochemical water splitting applications [49].

In Figs. 7 to 9, FESEM images of the different hybrid nanostructures are shown. Note that all the synthesized $TiO_2$-$WO_3$ nanostructures maintain the ordered and nanotubular structure possessed by pure $TiO_2$ nanotubes.

The sample electrodeposited at a concentration of 20 mM $H_2O_2$ and 5 mM $Na_2WO_4$ (Fig. 7a) shows a slight aggregation of $WO_3$ on the surface of the mouths of the nanotubes, in addition to tiny $WO_3$ particles arranged on the surface. As the concentration of $Na_2WO_4$ increases (Figs. 7b and 7c), the deposition of $WO_3$ on the nanotubes becomes more apparent.

It is important to highlight that the sample with an amount of 25 mM $Na_2WO_4$ and 20 mM $H_2O_2$ (Fig. 7c) shows a high electrodeposition of $WO_3$, covering practically the entire surface of the nanotubes. This will be a disadvantage in the subsequent photoelectrochemical water splitting since it may prevent the absorption of sunlight.

Regarding the nanostructures electrodeposited at 30 mM $H_2O_2$ (Fig. 8), the aggregation of $WO_3$ on the mouths of the nanotubes can also be observed, in addition to the presence of small particles of $WO_3$ deposited on the surface, especially in the samples synthesized at concentrations of 15 and 25 mM $Na_2WO_4$ (Figs. 8b and 8c). But, unlike the morphology presented when electrodeposition was performed at a concentration of 20 mM $H_2O_2$ (Fig. 7), in this case the $WO_3$ particles have not plugged the mouths of the nanotubes, in addition to having a slightly smaller size.

In the FESEM images obtained at a concentration of 40 mM $H_2O_2$ (Fig. 9), the presence of $WO_3$ on the surface is not so clearly appreciated, in addition to have fewer $WO_3$ particles than in the rest of the images. This is because if the $H_2O_2$ concentration is higher (40 mM), the $WO_3$ electrodeposition may be dissolved again [43].

All this can be justified based on the formation reactions of $WO_3$ (Eqs.5 to 7) since a higher concentration of $H_2O_2$ is able to dissolve $Na_2WO_4$ to a greater extent, transforming it to $[W_2O_{11}]^{-2}$ than in turn, dissociates to form $WO_3$, thus allowing a greater electrodeposition of this compound on the nanostructure. But at high concentrations of $H_2O_2$ (40 mM), once the $WO_3$ has been formed on the nanotubes, there is still the presence of $H_2O_2$ in the medium. This causes the complexation of $WO_3$ back to the intermediate compound $[W_2O_{11}]^{-2}$ (Eq.7).

For this reason, in Fig. 7 a greater electrodeposition of particles is observed when electrodeposition is carried out with 20 mM of $H_2O_2$, since this concentration is high enough to transform the intermediate compound $[W_2O_{11}]^{-2}$ to $WO_3$, but not as high as to complex back the formed $WO_3$. However, a slightly higher concentration such as 30 mM $H_2O_2$ is sufficient to dissolve some of the formed $WO_3$ and cause it to complex back to the intermediate compound, but it is not as high as 40 mM that occasionates that most of the deposited $WO_3$ converts again to $[W_2O_{11}]^{-2}$.

It is important to note that the nanostructures synthesized at a concentration of 5 mM of $Na_2WO_4$ and with a concentration of 30 and 40 mM of $H_2O_2$ (Figs. 7a and 8a) present a similar appearance. This is due to the fact that a low concentration of $Na_2WO_4$ provides a lower electrodeposition of $WO_3$, and despite the difference in the amount of $H_2O_2$, it can be assumed that the complexation of the $WO_3$ deposited with the intermediate compound will be similar under these conditions.

Therefore, despite the formation effect that $H_2O_2$ has on the electrodeposition process, it also presents the decomposition effect of $WO_3$ when its concentration in the medium is high.

To confirm the presence of $WO_3$ in each of the samples, especially in the nanostructures formed when electrodeposition was carried out at 40 mM of $H_2O_2$, an EDX analysis has been performed (Fig. 10). Figs. 10a and 10b shows, as an example, the EDX data of one of the spectra obtained for the sample electrodeposited in 5 mM $Na_2WO_4$ and 20 mM $H_2O_2$ and in 5 mM $Na_2WO_4$ and 40 mM $H_2O_2$, respectively. Additionally, Table 1 shows the data of different spectra taken in several areas of the hybrid nanostructures electrodeposited in the aforementioned conditions.

According to Fig. 10, the main elements detected in the samples are titanium, tungsten and oxygen, which confirms the presence of $WO_3$ in the nanostructures.

Spectrum 1 shows the concentration of a W particle (86.35 wt. %), which may block $TiO_2$ nanotubes. Table 1 shows that for the same amount of $Na_2WO_4$, the samples electrodeposited at a lower concentration of $H_2O_2$ present higher tungsten content in wt. %, since an increase in the concentration of hydrogen peroxide dissolves most of the electrodeposited $WO_3$ to intermediate $[W_2O_{11}]^{-2}$ (Eq. 7).

Besides, another spectrum was performed on the sample electrodeposited at 25 mM $Na_2WO_4$ and 30 mM $H_2O_2$ in order to determine the amount of tungsten electrodeposited at the highest amount of $Na_2WO_4$ (Fig. 10c). The titanium and tungsten wt. % obtained from this analysis were 79.83% and 20.17% respectively. Therefore, a higher concentration of $Na_2WO_4$ increases the amount of W present in the nanostructure (Table 1). Additionally, Fig. S1 shows, as an example, an EDX mapping of the nanostructure electrodeposited at 25 mM $Na_2WO_4$ and 30 mM $H_2O_2$, where an homogeneous Ti and W wt. % distribution can be observed.

*3.6. TEM Analysis*

Figure 11 shows HR-TEM images of the $TiO_2$-$WO_3$ sample electrodeposited at 25 mM $Na_2WO_4$ and 30 mM $H_2O_2$. It can be observed that $WO_3$ homogenously distributed along the nanotubes. Additionally, and according to the XRD patterns (Fig. 3), monoclinic (200) and (020) phases for $WO_3$ were found. On the other hand, for $TiO_2$, anatase (101) was also detected. Figure S2 reveals the presence of W for the samples electrodeposited with 5 and 15 mM of $Na_2WO_4$ and 30 mM $H_2O_2$.

*3.7. Photoelectrochemical response tests*

Photoelectrochemical response tests were carried out for each of the hybrid nanostructures, as well as an anodized $TiO_2$ nanostructure (without electrodeposition), that serves as a reference sample (Fig. 12)

During the test, photocurrent densities (i) are recorded as potential applied shift towards more positive values. At the same time, light pulses are applied: 60 mV in the dark and 20 mV with light. Fig. 12 shows that during the interval in which the light falls on the photocatalyst a significant increase in current density is observed. Regardless of the amounts of $Na_2WO_4$ and $H_2O_2$ electrodeposited, in most of the samples the current density improves compared to the sample of the pure $TiO_2$ (just anodized $TiO_2$ nanotubes). This is due to the incorporation of $WO_3$ to the nanostructure, which provides a narrowing of the bandgap induced by $WO_3$ [42], and might reduce the recombination of electron-hole ($e^-$ - $h^+$) pairs and a more effective charge separation. In the hybrid nanostructures, the electrons photogenerated in $TiO_2$ are transferred to the conduction band (BC) of $WO_3$, while the holes pass from the valence band of $WO_3$ to the $TiO_2$ [50]. Furthermore, the reduction in the recombination of the $e^-$ - $h^+$ pairs implies a greater

number of existing electrons for photoelectrochemical applications, such as, the photoelectrochemical water splitting.

Fig. 12 also shows that photocurrent densities increase as the potential shift towards more positive values, showing some stability at potential values of approximately 0.7 $V_{Ag/AgCl}$ in most of the samples. Besides, when light was switched off (dark conditions), the photocurrent density drops to values close to 0 $mA/cm^2$, which indicates a stability of the hybrid nanostructures. However, as the photoelectrode is illuminated again, the photocurrent densities increase rapidly to a constant value, which may be related to a rapid transport of the charges inside the photoelectrode [30].

Another aspect to consider is the peak that the different nanostructures present at the beginning of each pulse, which is mainly appreciated at potentials between 0.4-0.7 $V_{Ag/AgCl}$. This peak is related to recombination process of the electrons and holes generated. This process continues until a constant photocurrent density value is reached [51].

3.7.1. Influence of $H_2O_2$ and $Na_2WO_4$ content used for electrodeposition on the photoelectrochemical response

Figure 12 shows the photocurrents obtained for the different hybrid nanostructures. In particular, Figure 12a shows that nanostructures electrodeposited at the lowest $H_2O_2$ concentration (20mM) present the lowest photocurrent densities. This is because this concentration of $H_2O_2$ in the electrolyte is high enough as to dissolve the $Na_2WO_4$ molecule, especially at concentrations of 15 and 25mM $Na_2WO_4$, but it is also low enough as to redissolve part of the $WO_3$ formed back to the reaction intermediate $[W_2O_{11}]^{-2}$ (Eq.7), which causes the electrodeposition of a high amount of large $WO_3$ particles on the

surface of $TiO_2$ nanostructures, which can even plug the top of $TiO_2$ nanotubes and hinder the light absorption towards the photocatalyst surface. This effect is unfavourable for photoelectrochemical applications.

On the other hand, Figure 12b shows that the photocurrents obtained when electrodeposition was carried out at a concentration of 30 mM of $H_2O_2$ present the highest values and are considerably higher than the obtained for pure $TiO_2$ nanostructure (anodized without electrodeposition).

Besides, Figure 12c shows the photocurrent densities for the nanostructures electrodeposited with 40 mM $H_2O_2$. In this figure it can be observed how photocurrents decrease when the concentration of $Na_2WO_4$ is increased. This might be explained due to an excessive amount of $H_2O_2$ for the electrodeposition. That is, higher $H_2O_2$ contents together with higher $Na_2WO_4$ concentrations electrodeposited a higher amount of $WO_3$ on the nanostructure. But the higher concentration of $H_2O_2$ also exhibits the dissolution effect of the $WO_3$ formed, converting back to $[W_2O_{11}]^{-2}$. Therefore, under these conditions, a large amount of $WO_3$ is electrodeposited, which in turn decomposes the reaction intermediate again due to the fact that there is an excess of $H_2O_2$ in the medium, thus providing less $WO_3$ particles on the nanostructure.

Nevertheless, when samples are electrodeposited with the lowest concentration of $Na_2WO_4$ (5 mM), higher photocurrents are obtained, especially for the 20 and 40 mM $H_2O_2$ concentrations (Figure 12a and 12b). In this way, a lower $Na_2WO_4$ concentration allows the deposition of a less amount of $WO_3$, which prevents the clogging of the mouths of the nanotubes and may allow absorption of light by the samples.

Note that for the hybrid nanostructures electrodeposited 30 mM $H_2O_2$ concentrations (Figure 12b), photocurrents are very similar, regardless the $Na_2WO_4$ concentration,

showing all of them favourable photoelectrochemical behavior for water splitting applications. This could be explained since a concentration of 30 mM $H_2O_2$ is high enough to dissolve the $Na_2WO_4$ necessary for $WO_3$ electrodeposition, but it is not so high as to complex again the $WO_3$ electrodeposited particles. For the photoelectrochemical response of the hybrid nanostructures at this particular concentration (which presented the best photocurrent densities for water splitting), other authors [52-54] obtained similar or lower photocurrent densities at ~0.55 $V_{Ag/AgCl}$ (which was the potential at which the highest photocurrents were obtained in the present study). Even in these studies, the hybrid $TiO_2$-$WO_3$ nanostructures were prepared by hydrothermal methods (with the disadvantages of: long time, use of different reagents, temperature, use of an autoclave…) and on an FTO conductive glass, which may increase the obtained photocurrents. Additionally, some of these studies tested the heterostructures with an incident light intensity of 320 mW/cm$^2$ (three times higher than the one used in the present paper).

In summary, according to photoelectrochemical response tests, an excess of $WO_3$ in the nanostructures provides lower photocurrents for water splitting, since the area of the photoanode is covered of particles which hinder light absorption [34].

Stability tests performed to the samples under illumination and at 1 $V_{Ag/AgCl}$ for 1h revealed that photocatalyst were stable. Moreover, E-i curves both with light and under dark conditions after the tests revealed that samples were stable. Besides, the morphology and the crystalline structure of the samples was maintained after the tests (see Fig. S3).

*3.7.2.* Statistical analysis

Table 2 shows the analysis of the Variance for the photocurrents obtained from the statistical design. None of the effects result statistically significant for photoelectrochemical water splitting, since their p-values were higher than 0.05.

However, the p-value for the interaction between $Na_2WO_4$ and $H_2O_2$ was almost significant (p-value = 0.0516). Besides the quadratic effect of $Na_2WO_4$ have a p-value considerably higher than 0.05 (0.4809), therefore, it was excluded from the analysis (see Figures 13a and 13b). It is noticeable that the simple effect of $Na_2WO_4$ concentration was not excluded from the analysis since the interaction between $Na_2WO_4$ and $H_2O_2$ was almost statistically significant. The new analysis (excluding the quadratic effect of $Na_2WO_4$ concentration) is shown in Table 3 and Figure 13b. Table 3 shows that when the quadratic effect of $Na_2WO_4$ concentration was excluded the interaction between $Na_2WO_4$ and $H_2O_2$ concentration results statistically significant (p-value of 0.0459). As a consequence of this, in order to fabricate the most suitable hybrid nanostructures (higher photocurrent densities), it is not only important to fix the $Na_2WO_4$ concentration, but also the $H_2O_2$ amount. This is because higher $Na_2WO_4$ concentrations are appropriate for photoelectrochemical applications when 30 mM of $H_2O_2$ concentration is used for electrodeposition. However, low photocurrent responses are obtained at higher $Na_2WO_4$ when electrodeposition is performed at 20 and 40 mM. This explains the statistical significance of the interaction between $Na_2WO_4$ and $H_2O_2$ concentrations.

## 4. CONCLUSIONS

Hybrid $TiO_2$-$WO_3$ nanostructures were synthesized by electrochemical anodization under hydrodynamic conditions followed by electrodeposition at different $H_2O_2$ and $Na_2WO_4$ concentrations.

FESEM revealed the formation of ordered nanotubes with different morphologies depending on the $H_2O_2$ and $Na_2WO_4$ content. XPS, HR-TEM, XRD, Raman spectroscopy and EDX confirm the presence of $WO_3$ in the nanostructures. Additionally, AFM

demonstrates the increase in roughness in the hybrid samples if compared to the $TiO_2$ one.

Statistical analysis reveals that the interaction between $Na_2WO_4$ and $H_2O_2$ concentrations is statistically significant since high $Na_2WO_4$ contents are appropriated when electrodeposition is performed at 30 mM $H_2O_2$. On the contrary, with 20 and 40 mM $H_2O_2$ contents and high $Na_2WO_4$ concentrations low photocurrents are obtained. This is because a concentration of 30 mM of $H_2O_2$ allows the electrodeposition of a certain $WO_3$ amount which makes it possible to enhance the photoelectrochemical water splitting. In fact, nanostructures synthesized under these conditions (30 mM $H_2O_2$) were the best photocatalysts in terms of higher photocurrent densities for water splitting, with an increase in the photocurrent of 50-60 % with respect to the $TiO_2$ nanotubes.

**Aknowledgements**

Authors thank for the financial support to the Generalitat Valenciana (Project Code: GV/2020/044) as well as to the project co-funded by FEDER operational programme 2014-2020 of Comunitat Valenciana (IDIFEDER/18/044). Authors also thank the Ministerio de Ciencia e Innovación (Project Code: PID2019-105844RB-I00), for its help in the Laser Raman Microscope acquisition (UPOV08-3E-012) and for the co-finance by the European Social Fund. Authors also thank Alicia Mestre and Said Agouram from the SCSIE (Universitat de València) for their help with the XRD and HR-TEM measurements.

## REFERENCES


[1] J. D. Fonseca, M. Camargo, J. M. Commenge, L. Falk, and I. D. Gil, “Trends in design of distributed energy systems using hydrogen as energy vector: A systematic literature review,” *Int. J. Hydrogen Energy* 44 (2019) 9486-9504.

[2] S. Ashrafi, M. Mousavi-Kamazani, S. Zinatloo-Ajabshir, A. Asghari, “Novel sonochemical synthesis of $Zn_2V_2O_7$ nanostructures for electrochemical hydrogen storage” *Int. J. Hydrogen Energy* 45 (2020) 21611-21624.

[3] M. Masjedi-Arani, M. Ghiyasian-Arani, O. Amiri, M. Salavati-Niassari, “CdSnO3-graphene nanocomposites: ultrasonic synthesis using glucose as capping agent and characterization for electrochemical hydrogen storage” Ultrason Sonochem, 61 (2020) 104840-104852.

[4] S.B. Patil, P.S.Basavarajappa, N. Ganganagappa, M.S. Jyothi, A.V. Raghu, K.R. Reddyd, “Recent advances in non-metals-doped $TiO_2$ nanostructured photocatalysts for visible-light driven hydrogen production, $CO_2$ reduction and air purification” *Int. J. Hydrogen Energy* 44 (2019) 13022-13039.

[5] M. D. Cabezas, A. E. Frak, A. Sanguinetti, J. I. Franco, and H. J. Fasoli, “Hydrogen energy vector: Demonstration pilot plant with minimal peripheral equipment,” *Int. J. Hydrogen Energy* 39 (2014) 18165–18172.

[6] Š.Kment K.Sivula, A.Naldoni, S.P.Sarmah, H.Kmentová, M.Kulkarni, Y.Rambabu, P.Schmuki, R.Zbořil, “FeO-based nanostructures and nanohybrids for photoelectrochemical water splitting” *Progress in Materials Science* 110 (2020) 100632-100688.

[7] S. Shiva Kumar and V. Himabindu, “Hydrogen Production by PEM Water Electrolysis – A Review,” *Mater. Sci. Energy Technol.*. 2 (2019) 442-454.

[8] P. Nikolaidis and A. Poullikkas, “A comparative overview of hydrogen production processes,” *Renew. Sustain. Energy Rev.* 67 (2017) 597–611.

[9] B. Y. Alfaifi, H. Ullah, S. Alfaifi, A. A. Tahir, and T. K. Mallick, “Photoelectrochemical solar water splitting: From basic principles to advanced devices,” *Veruscript Funct. Nanomater.* 2 (2018) BDJOC3.

[10] C. Fleischer, A. Chatzitakis, and T. Norby, “Intrinsic photoelectrocatalytic activity in oriented, photonic $TiO_2$ nanotubes” *Mater. Sci. Semicond. Process.* 88 (2018) 186–191.

[11] S. K. Saraswat, D. D. Rodene, and R. B. Gupta, “Recent advancements in semiconductor materials for photoelectrochemical water splitting for hydrogen production using visible light” *Renew. Sustain. Energy Rev.* 89 (2018) 228–248.

[12] P. Roy, S. Berger, and P. Schmuki, “$TiO_2$ nanotubes: Synthesis and applications” *Angew. Chemie - Int. Ed.* 50 (2011) 2904–2939.

[13] A. Chatzitakis, A. Papaderakis, N. Karanasios, J. Georgieva, E. Pavlidou, G. Litsardakis, I. Poulios, S. Sotiropoulos, “Comparison of the photoelectrochemical performance of particulate and nanotube $TiO_2$ photoanodes,” *Catal. Today* 280 (2017) 14–20.

[14] S. Shen, J. Chen, M. Wang, X. Sheng, X. Chen, X. Feng, S.S. Mao., “Titanium dioxide nanostructures for photoelectrochemical applications,” *Prog. Mater. Sci.* 98 (2018) 299–385.

[15] C. W. Lai and S. Sreekantan, “Effect of heat treatment on $WO_3$-loaded $TiO_2$ nanotubes for hydrogen generation via enhanced water splitting,” *Mater. Sci. Semicond. Process.* 16 (2013) 947–954.

[16] K. Indira, U. K. Mudali, T. Nishimura, and N. Rajendran, “A Review on $TiO_2$ Nanotubes: Influence of Anodization Parameters, Formation Mechanism, Properties, Corrosion Behavior, and Biomedical Applications” *J. Bio- Tribo-Corrosion* 1 (2015) 1–22.

[17] M.A. Bin Adnan, K. Arifin, L.J. Minggu, M.B. Kassim, “Titanate-based perovskites for photochemical and photoelectrochemical water splitting applications: a review” *Int J Hydrogen Energy* 43 (2018) 23209-23220.

[18] M. M. Momeni, Y. Ghayeb, and M. Davarzadeh, “Single-step electrochemical anodization for synthesis of hierarchical $WO_3$-$TiO_2$ nanotube arrays on titanium foil as a good photoanode for water splitting with visible light” *J. Electroanal. Chem.* 739 (2015) 149–155.

[19] Y. Ma, X. Wang, Y. Jia, X. Chen, H. Han, and C. Li, “Titanium Dioxide-Based Nanomaterials for Photocatalytic Fuel Generations” *Chem. Rev.* 114 (2014) 9987–10043.

[20] M.M Momeni, Y. Ghayeb, “Preparation ofcobaltcoated$TiO_2$ and $WO_3$–$TiO_2$ nanotube films via photo-assisted deposition with enhanced photocatalytic activity under visible light illumination” *Ceram. Int.* 42 (2016) 7014–7022.

[21] M.M Momeni, Y. Ghayeb, M. Davarzadeh “$WO_3$ nanoparticles anchored on titania nanotube films as efficient photoanodes” *Surf. Eng31 (2015) 259-264.*

[22] Y. Wang, F. Zhang, G. Zhao, Y. Zhao, Y. Ren, H. Zhang, L. Zhang, J. Du, Y. Han, D.J. Kang, "Porous $WO_3$ monolith-based photoanodes for high-efficient photoelectrochemical water splitting" *Ceram. Int.* 45 (2019) 7302–7308.

[23] S. Caramori, V. Cristino, L. Meda, A. Tacca, R. Argazzi, and C. A. Bignozzi, "Efficient anodically grown $WO_3$ for photoelectrochemical water splitting" *Energy Procedia*, vol. 22 (2011) 127–136.

[24] M. Zlamal and J. Krysa, "Photo-electrochemical properties of $WO_3$ particulate layers," *Catal. Today* 252 (2015) 162–167.

[25] A. Ghicov and P. Schmuki, "Self-ordering electrochemistry: A review on growth and functionality of $TiO_2$ nanotubes and other self-aligned MOx structures," *Chem. Commun.* 20 (2009) 2791–2808.

[26] D. Regonini, C. R. Bowen, A. Jaroenworaluck, and R. Stevens, "A review of growth mechanism, structure and crystallinity of anodized $TiO_2$ nanotubes" *Mater. Sci. Eng. R Reports* 74 (2013) 377–406.

[27] M.M Momeni, Y. Ghayeb, "Photoinduced deposition of gold nanoparticles on $TiO_2$–$WO_3$ nanotube films as efficient photoanodes for solar water splitting" *Appl. Phys. A* (2016) 122:620.

[28] M.M Momeni, Z. Nazari, "Preparation of $TiO_2$ and $WO_3$–$TiO_2$ nanotubes decorated with PbO nanoparticles bychemical bath deposition process: A stable and efficient photocatalyst" *Ceram. Int.* 42 (2016) 8691-8697.

[29] M. Bendova, F. Gispert-Guirado, A. Walter-Hassel, E. Llobet, A. Mozalev, "Solar water splitting on porous-alumina-assisted $TiO_2$-doped $WO_x$ nanorod photoanodes: Paradoxes and challenges" *Nano Energy* 33 (2017) 72–87.

[30] C. W. Lai and S. Sreekantan, “Preparation of hybrid $WO_3$-$TiO_2$ nanotube photoelectrodes using anodization and wet impregnation: Improved water-splitting hydrogen generation performance” *Int. J. Hydrogen Energy* 38 (2013) 2156–2166.

[31] S. Girish-Kumar, K.S.R. Koteswara-Rao, “Comparison of modification strategies towards enhanced chargecarrier separation and photocatalytic degradation activity of metaloxide semiconductors ($TiO_2$, $WO_3$and ZnO)” *Appl. Surf. Sci. 391 (2017) 124–148*.

[32] W. H. Lee, C. W. Lai, and S. B. A. Hamid, “One-step formation of $WO_3$-loaded $TiO_2$ nanotubes composite film for high photocatalytic performance” *Materials (Basel)* 8 (2015) 2139–2153.

[33] M. Nazari, F. Golestani-Fard, R. Bayati, and B. Eftekhari-Yekta, “Enhanced photocatalytic activity in anodized $WO_3$-loaded $TiO_2$ nanotubes” *Superlattices Microstruct.* 80 (2015) 91–101.

[34] K. R. Reyes-Gil and D. B. Robinson, “$WO_3$-enhanced $TiO_2$ Nanotube Photoanodes for Solar Water Splitting with Simultaneous Wastewater Treatment” *ACS Appl. Mater. Interfaces* 5 (2013) 12400–12410.

[35] K. R. Reyes-Gil, Z. D. Stephens, V. Stavila, and D. B. Robinson, “Composite $WO_3$/$TiO_2$ Nanostructures for High Electrochromic Activity” *ACS Appl. Mater. Interfaces* 7 (2015) 2202–2213.

[36] H. Ali, N. Ismail, A. Hegazy, and M. Mekewi, “A novel photoelectrode from $TiO_2$-$WO_3$ nanoarrays grown on FTO for solar water splitting” *Electrochim. Acta* 150 (2014) 314–319.

[37] A. S. Martins, P. J. M. Cordeiro-Junior, G. G. Bessegato, J. F. Carneiro, M. V. B.

Zanoni, and M. R. de V. Lanza, “Electrodeposition of $WO_3$ on Ti substrate and the influence of interfacial oxide layer generated in situ: A photoelectrocatalytic degradation of propyl paraben” *Appl. Surf. Sci.* 464 (2019) 664–672.

[38] N. A. Ramos-Delgado, M. A. Gracia-Pinilla, L. Maya-Treviño, L. Hinojosa-Reyes, J. L. Guzman-Mar, and A. Hernández-Ramírez, “Solar photocatalytic activity of TiO2 modified with WO3 on the degradation of an organophosphorus pesticide” *J. Hazard. Mater.* 263 (2013) 36–44.

[39] C. W. Lai, “$WO_3$-$TiO_2$ Nanocomposite and its Applications: A Review,” *Nano Hybrids Compos.* 20 (2018) 1–26.

[40] M. Shakeel Ahmad, A. K. Pandey, and N. Abd Rahim, “Advancements in the development of $TiO_2$ photoanodes and its fabrication methods for dye sensitized solar cell (DSSC) applications. A review” *Renew. Sustain. Energy Rev.* 77 (2017) 89–108.

[41] F. Khatun, A. A. Aziz, A. K. M. Kafi, and S. L. Ching, “Synthesis and Characterization of TiO 2 Nanotube Using Electrochemical Anodization Method” *Int. J. Eng. Tech. Sci.* 5 (2018) 132–139.

[42] N. F. A. B. Harun, Y. bin Mohd, L. Y. Pei, and L. Y. Chin, “Fabrication of tungsten trioxide-loaded titania nanotubes as a potential photoanode for photoelectrochemical cell” *Int. J. Electrochem. Sci.* 13 (2018) 5041–5053.

[43] R. M. Fernández-Domene, R. Sánchez-Tovar, B. Lucas-Granados, G. Roselló-Márquez, and J. García-Antón, “A simple method to fabricate high-performance nanostructured $WO_3$ photocatalysts with adjusted morphology in the presence of complexing agents” *Mater. Des.* 116 (2017) 160–170.

[44] S.A. Abdullah, M.Z. Sahdan, N. Nayan, Z. Embong, C. Rohaida, F. Adriyanto, "Neutron beam interaction with rutile $TiO_2$ single crystal (1 1 1): Raman and XPS study on $Ti^{3+}$-oxygen vacancy formation" *Mat. Lett.* 263 (2020) 127143.

[45] S.A. Abdullah, M.Z. Sahdan, N. Nafarizal, H. Saim, Z. Embong, C.H. Cik Rohaida, F.Adriyanto, "Influence of substrate annealing on inducing $Ti^{3+}$ and oxygen vacancy in $TiO_2$ thin films deposited via RF magnetron sputtering" *Appl. Surf. Sci* 462 (2018) 575–582.

[46] H. Guo, N. Jiang, H. Wang, N. Lu, K. Shang, J. Li, Y. Wu, "Degradation of antibiotic chloramphenicol in water by pulsed discharge plasma combined with $TiO_2$/$WO_3$ composites: mechanism and degradation pathway" *J. Hazard. Mat.* 371 (2019) 666–676.

[47] M Penza, M.A Tagliente, L. Mirenghi, C. Gerardi, C. Martucci, G. Cassano, "Tungsten trioxide ($WO_3$) sputtered thin films for a $NO_x$ gas sensor" *Sensors and Actuators B: Chem.* 50 (1998) 9–18.

[48] C. B. D. Marien, T. Cottineau, D. Robert, and P. Drogui, "$TiO_2$ Nanotube arrays: Influence of tube length on the photocatalytic degradation of Paraquat" *Appl. Catal. B Environ.* 194 (2016) 1–6.

[49] A. Mazzarolo, K. Lee, A. Vicenzo, and P. Schmuki, "Anodic $TiO_2$ nanotubes: Influence of top morphology on their photocatalytic performance" *Electrochem. commun.* 22 (2012) 162–165.

[50] O. Vozniuk, N. Tanchoux, J. M. Millet, S. Albonetti, F. Di Renzo, and F. Cavani, "Spinel Mixed Oxides for Chemical-Loop Reforming: From Solid State to Potential Application*" Studies in Surf. Sci. and Cat.* 178 (2019) 281-302.

[51] D. Tafalla, P. Salvador, and R. M. Benito, “Kinetic Approach to the Photocurrent Transients in Water Photoelectrolysis at n-$TiO_2$ Electrodes” 137 (1990) 1810–1815.

[52] S. Lin, H. Ren, Z. Wu, L. Sun, X.G. Zhang, Y.M. Lin, K.H. L. Zhang, C.J. Lin, Z.Q. Tian, J.F. Li, “Direct Z-scheme $WO_3$-x nanowire-bridged $TiO_2$ nanorod arrays for highly efficient photoelectrochemical overall water splitting” *J. Energy Chem.* 59 (2021) 721–729.

[53] H. Ali, N. Ismail, A. Hegazy, M. Mekewi, “A novel photoelectrode from $TiO_2$-$WO_3$ nanoarrays grown on FTO for solar water splitting” *Electrochim. Acta* 150 (2014) 314–319.

[54] I.A. Castro, G. Byzynski, M. Dawson, C. Ribeiro, “Charge transfer mechanism of $WO_3$/$TiO_2$ heterostructure for photoelectrochemical water splitting” *J. Photochem. Photobiol. A-Chem.* 339 (2017) 95–102.

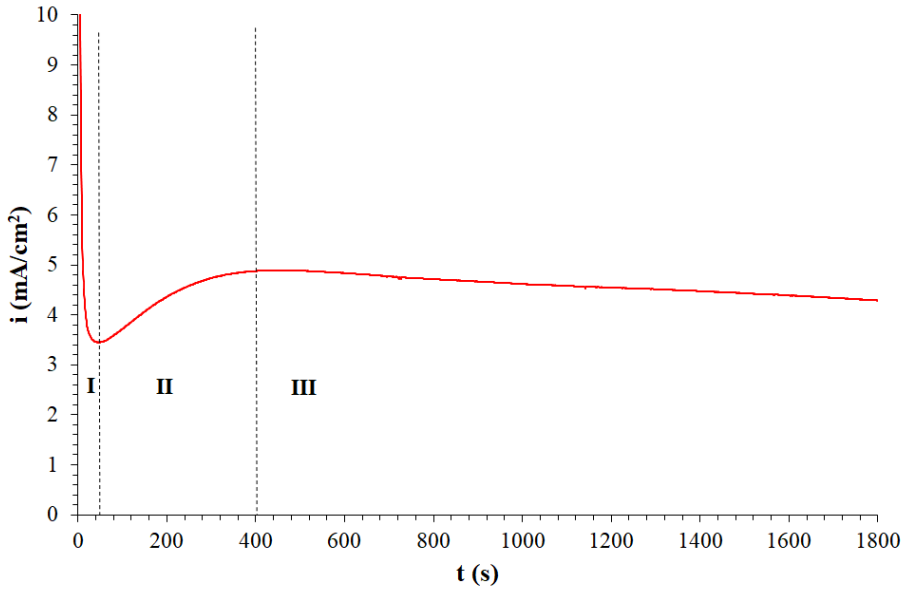


**Figure 1**. Current densities vs time during anodization of titanium at 55 V for 30 min and stirring the electrode at 3000 rpm.

**a) 20 mM $H_2O_2$**

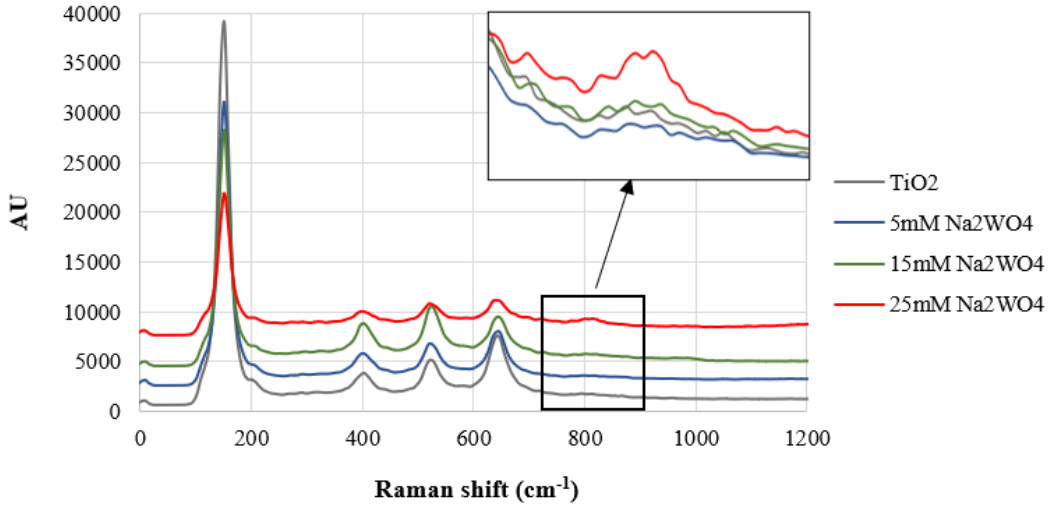


**b) 30 mM $H_2O_2$**

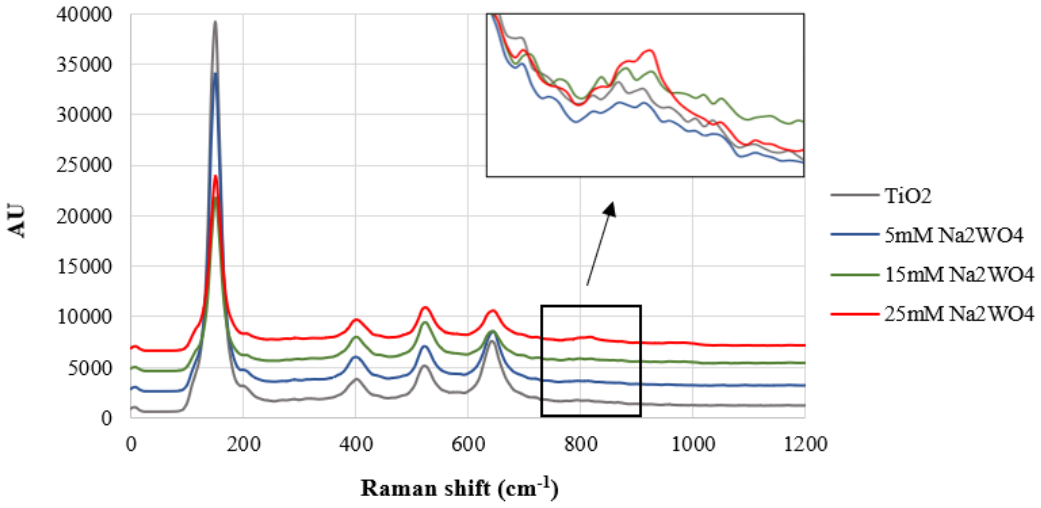


**c) 40 mM $H_2O_2$**

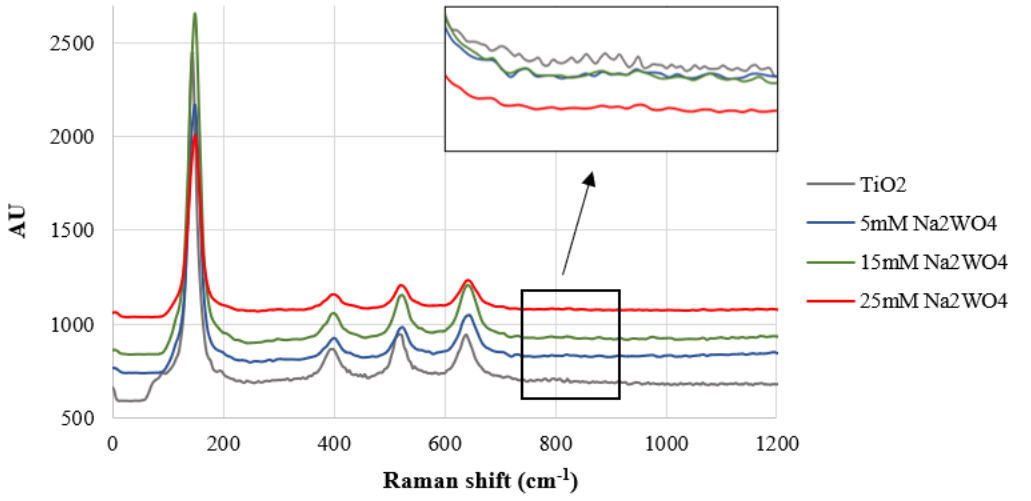

**Figure 2.** Raman spectra for the $TiO_2$ nanostructure and the different hybrid nanostructures electrodeposited with a) 20 mM $H_2O_2$ at 5, 15 and 25 mM of $Na_2WO_4$, b) 30 mM $H_2O_2$ at 5, 15 and 25 mM of $Na_2WO_4$ and c) 40 mM $H_2O_2$ at 5, 15 and 25 mM of $Na_2WO_4$.

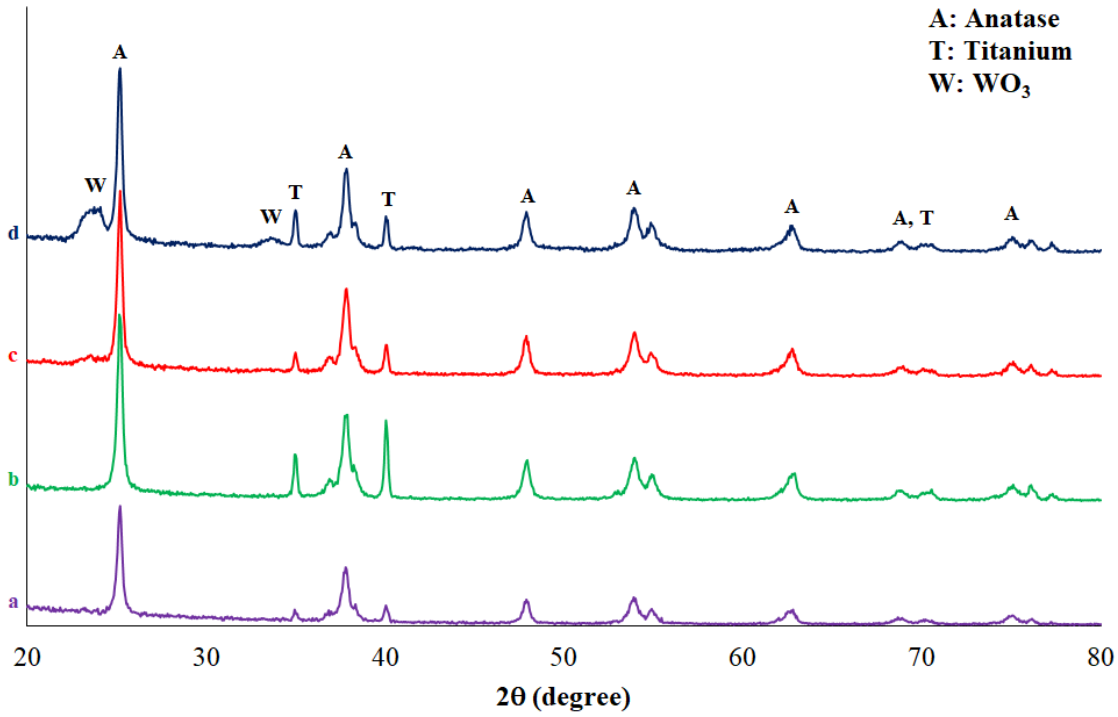


**Figure 3**. XRD patterns of a: $TiO_2$ and b: $TiO_2$-$WO_3$ 5 mM $Na_2WO_4$-30 mM $H_2O_2$, c: $TiO_2$-$WO_3$ 15 mM $Na_2WO_4$-30 mM $H_2O_2$ and d: $TiO_2$-$WO_3$ 25 mM $Na_2WO_4$-30 mM $H_2O_2$.

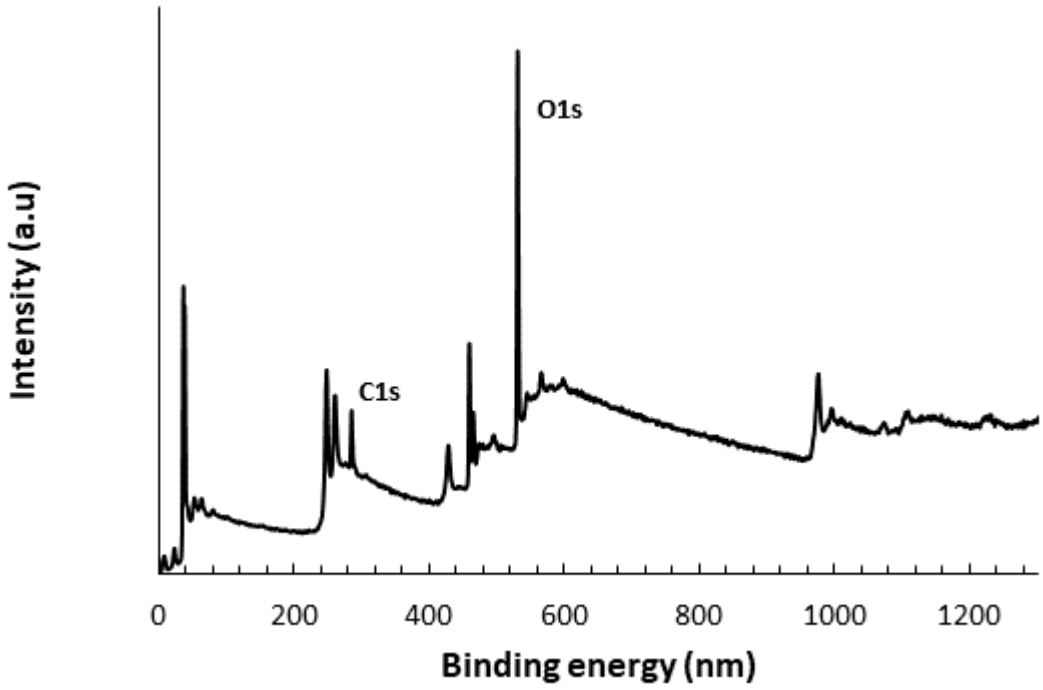


**Figure 4.** XPS Spectra of the $TiO_2$-$WO_3$ nanostructure electrodeposited with 25 mM $Na_2WO_4$ and 30 mM $H_2O_2$.

a)

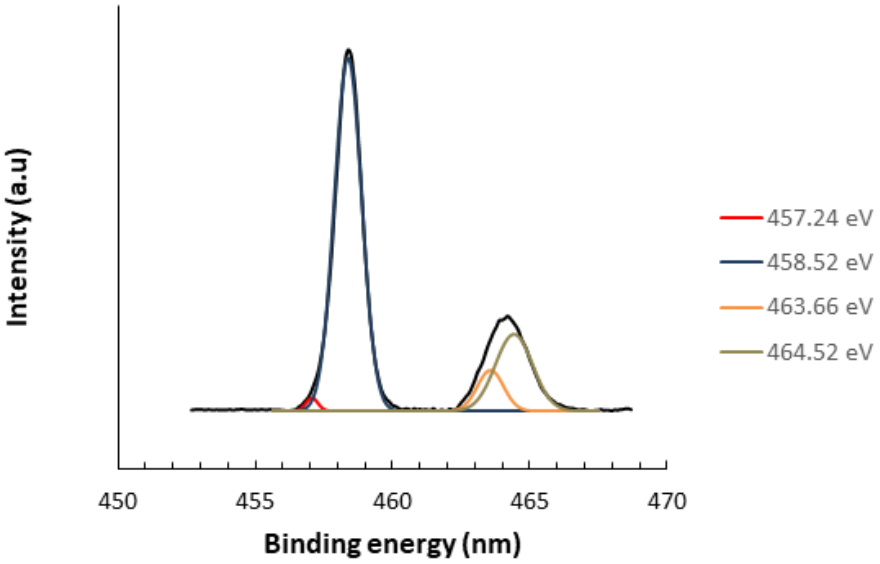
Intensity (a.u)
450
455
460
465
470
Binding energy (nm)
457.24 eV
458.52 eV
463.66 eV
464.52 eV

b)

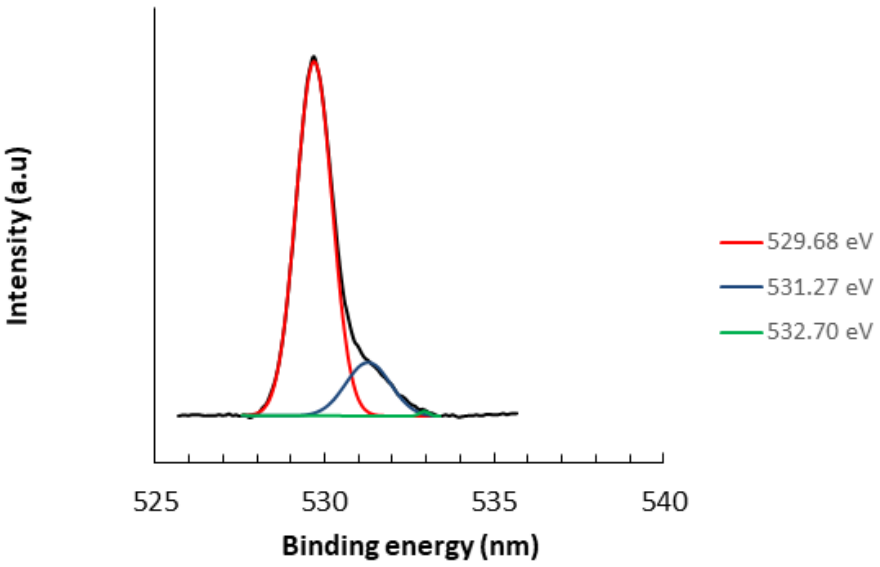
Intensity (a.u)
525
530
535
540
Binding energy (nm)
529.68 eV
531.27 eV
532.70 eV

c)

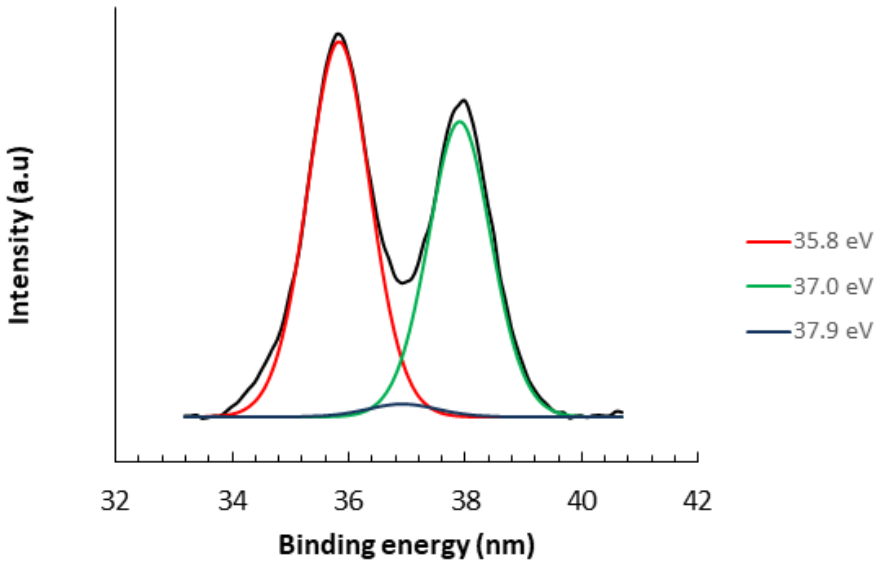


**Figure 5.** XPS Spectra of the $TiO_2$-$WO_3$ nanostructure electrodeposited with 25 mM $Na_2WO_4$ and 30 mM $H_2O_2$: Ti 2p (a), O 1s (b) and W 4f (c)

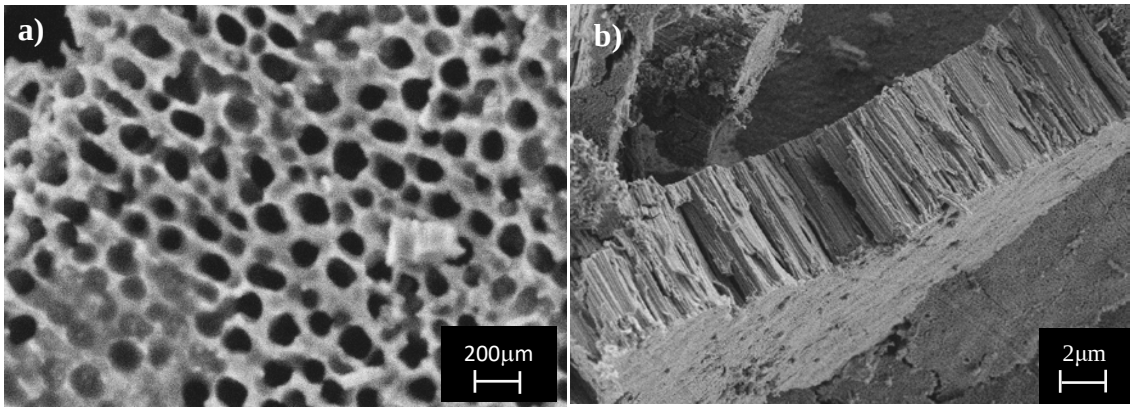


**Figure 6**. a) FE-SEM image of the surface of the $TiO_2$ nanotubes at 30,000X. b) FE-SEM image of the cross section of the $TiO_2$ nanotubes at 5,000X.

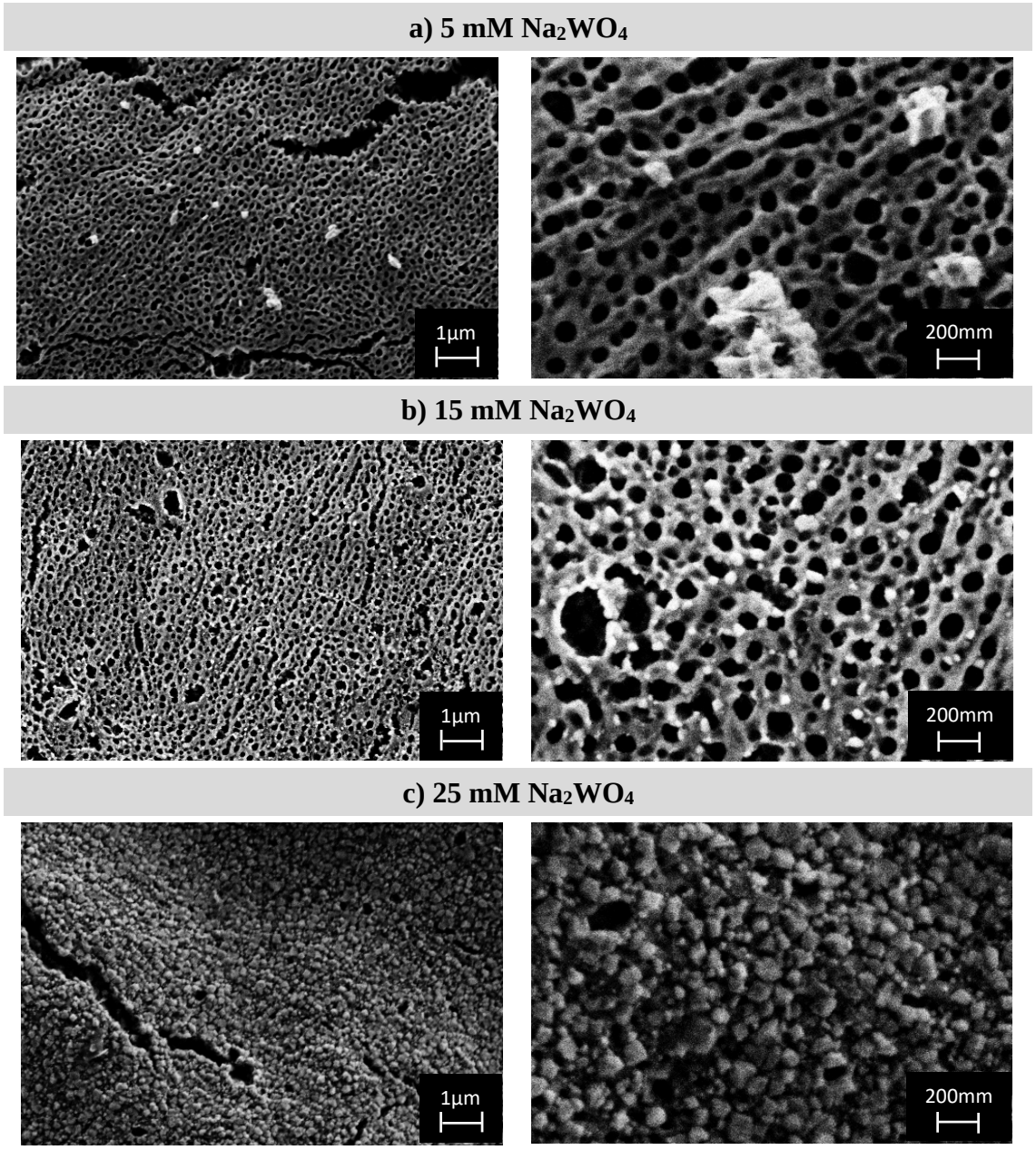


**Figure 7**. FE-SEM images of the nanotubes electrodeposited at 20mM $H_2O_2$ with different amounts of $Na_2WO_4$.

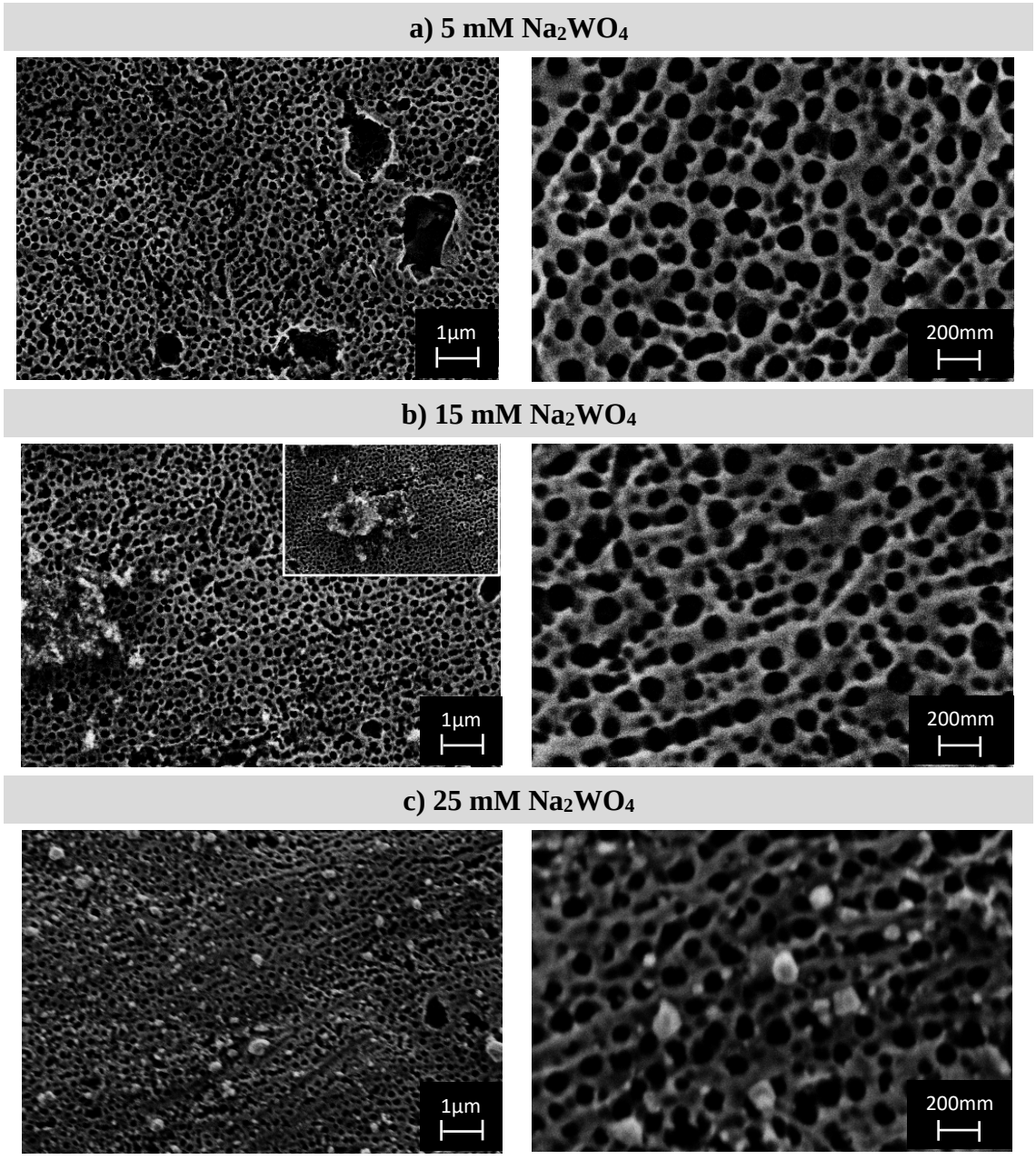


**Figure 8**. FE-SEM images of the nanotubes electrodeposited at 30mM $H_2O_2$ with different amounts of $Na_2WO_4$.

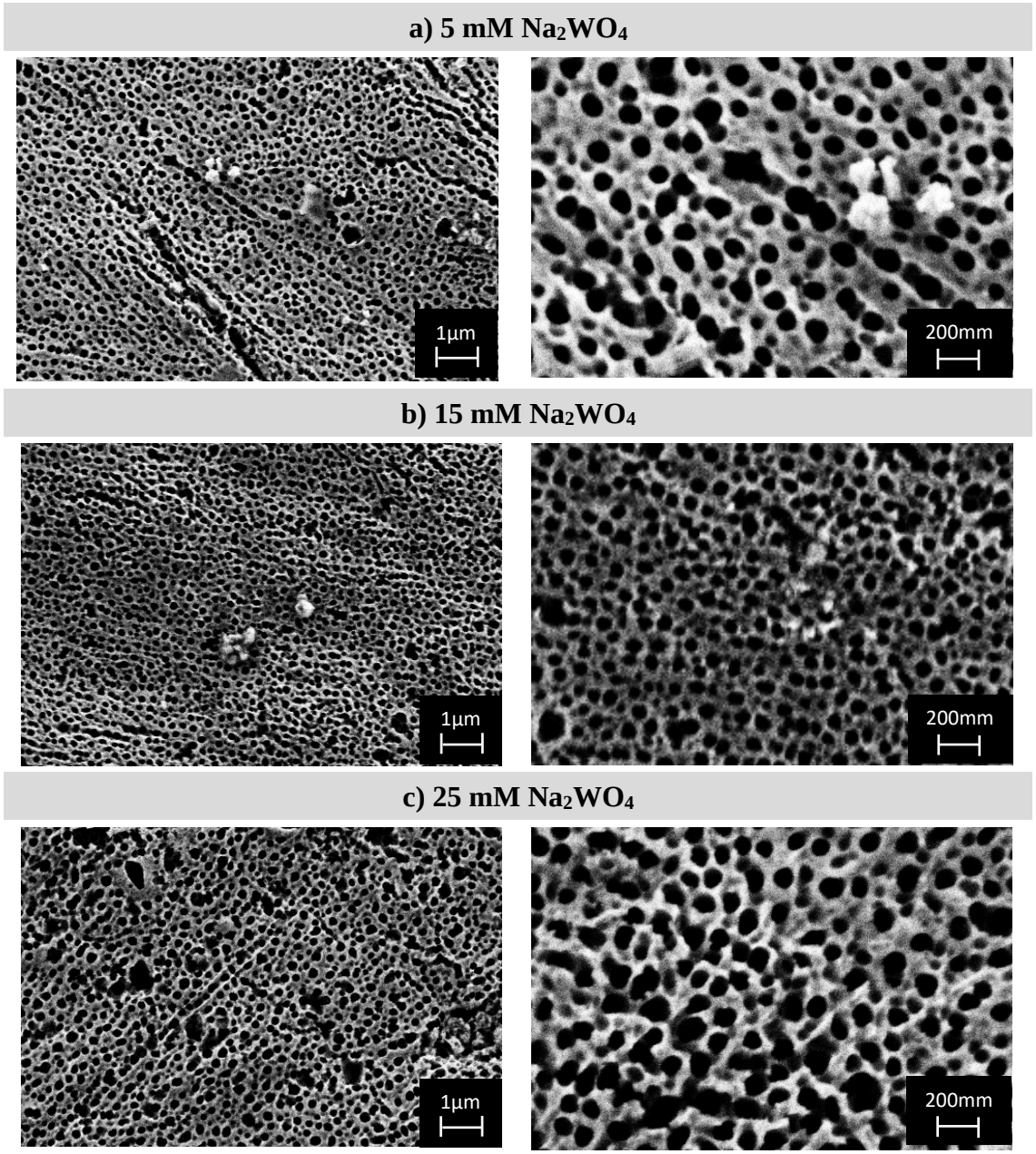


**Figure 9**. FE-SEM images of the nanotubes electrodeposited at 40mM $H_2O_2$ with different amounts of $Na_2WO_4$.

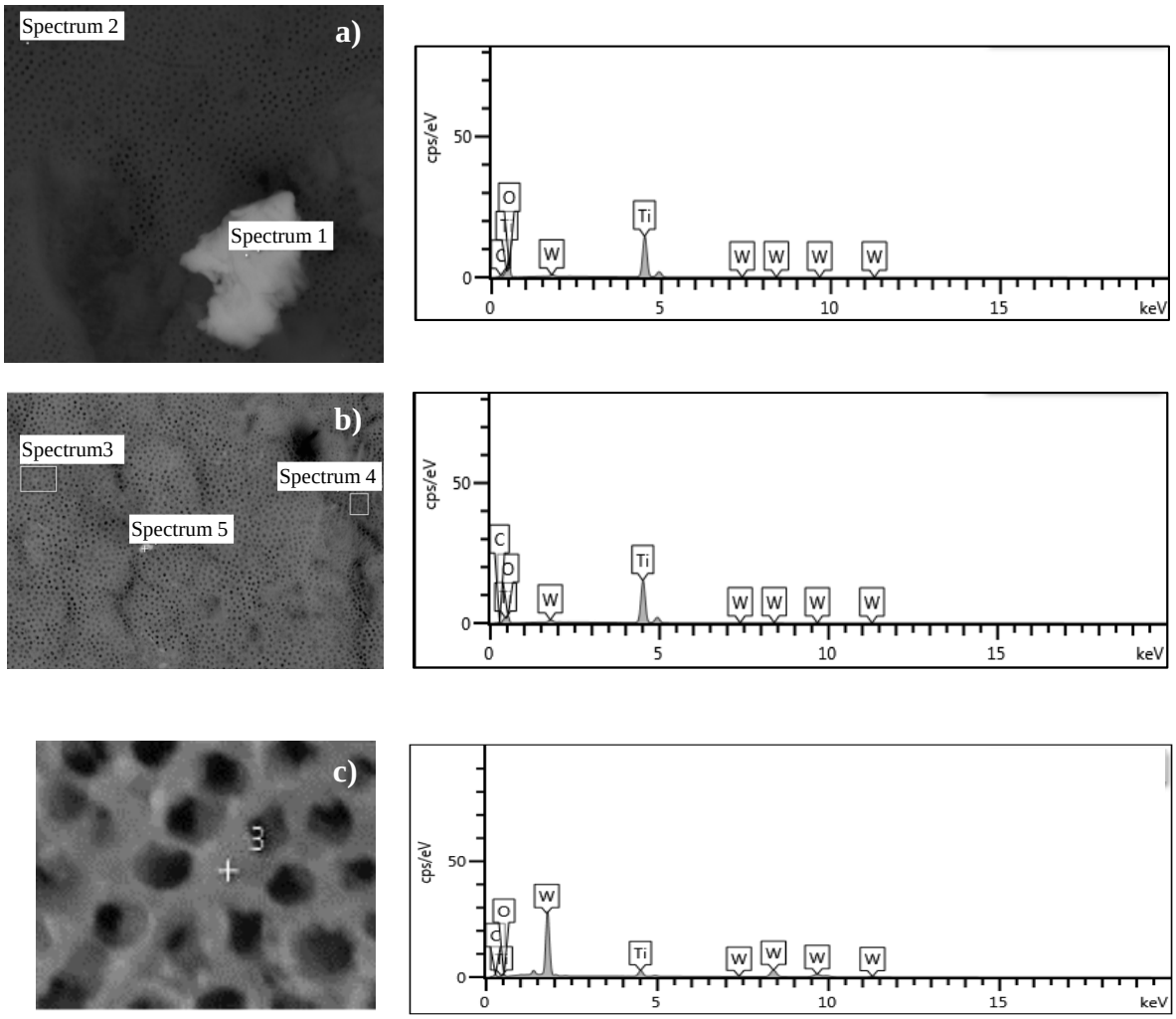


**Figure 10**. Image and EDX spectrum of the nanostructures electrodeposited with 5mM $Na_2WO_4$ and a) 20mM $H_2O_2$, b) 40mM $H_2O_2$. And c) EDX spectrum of the nanostructures electrodeposited with 25mM $Na_2WO_4$ and 30mM $H_2O_2$.

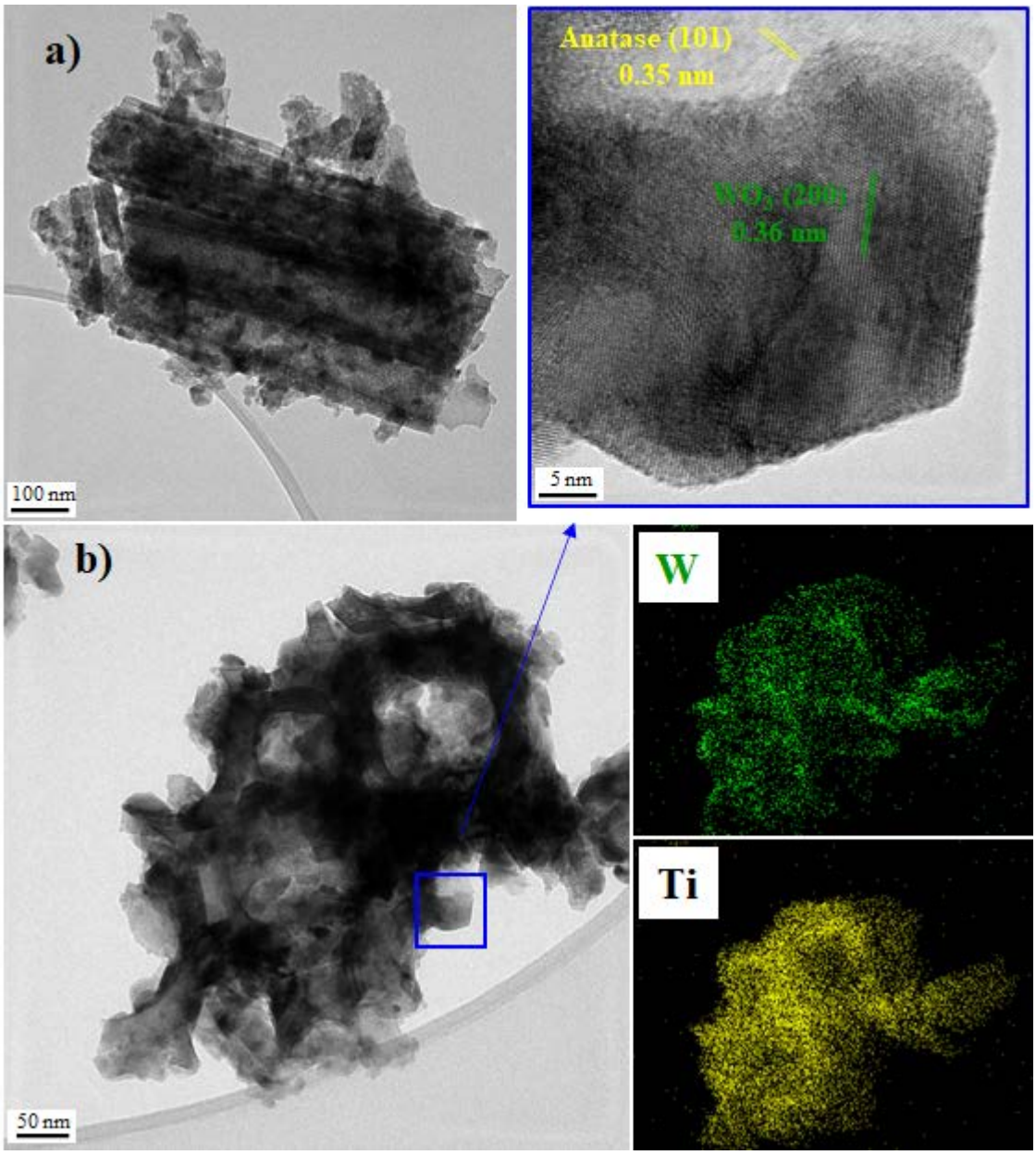


**Figure 11**. HR-TEM images of the TiO2-WO3 nanostructure electrodeposited at 25 mM Na2WO4 and 30mM $H_2O_2$. a) Vertical view of the nanotubes. b) Horizontal view of the nanotubes.

**a) 20 mM $H_2O_2$**

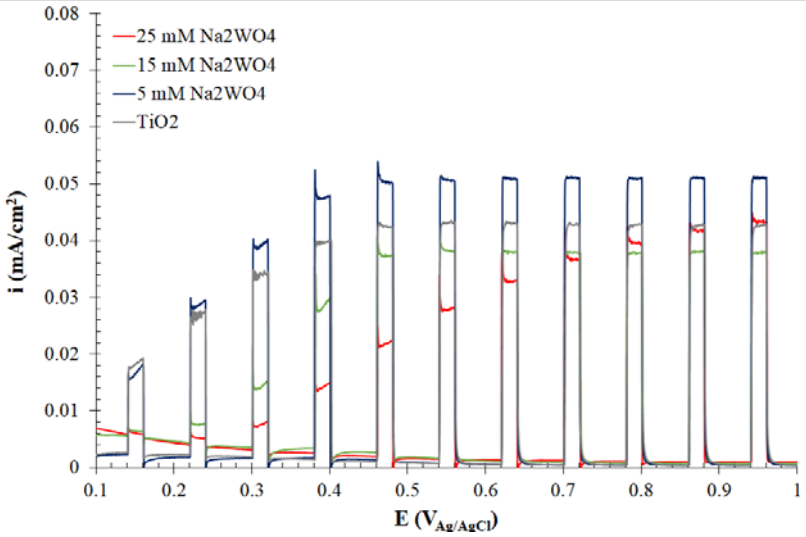


**b) 30 mM $H_2O_2$**

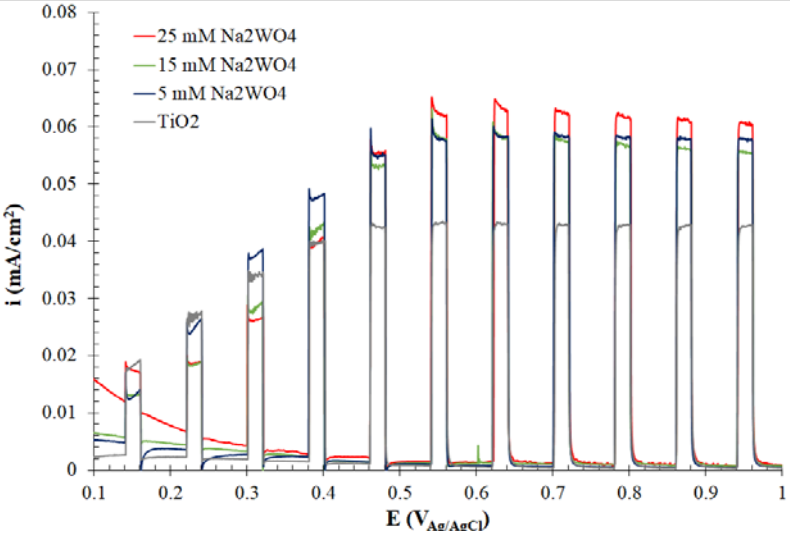

**c) 40 mM $H_2O_2$**

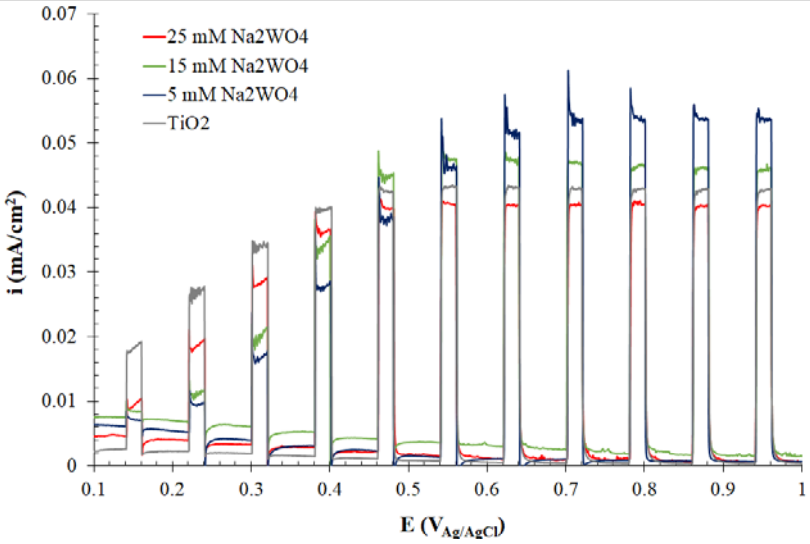


**Figure 12.** Current density vs. applied potential curves under dark and illumination conditions (AM 1.5) for the $TiO_2$ nanostructures together with the different hybrid nanostructures electrodeposited with 20 mM $H_2O_2$ at 5, 15 and 25 mM of $Na_2WO_4$ a) 30 mM $H_2O_2$ at 5, 15 and 25 mM of $Na_2WO_4$ b) and 40 mM $H_2O_2$ at 5, 15 and 25 mM of $Na_2WO_4$ c).

a) Pareto Chart

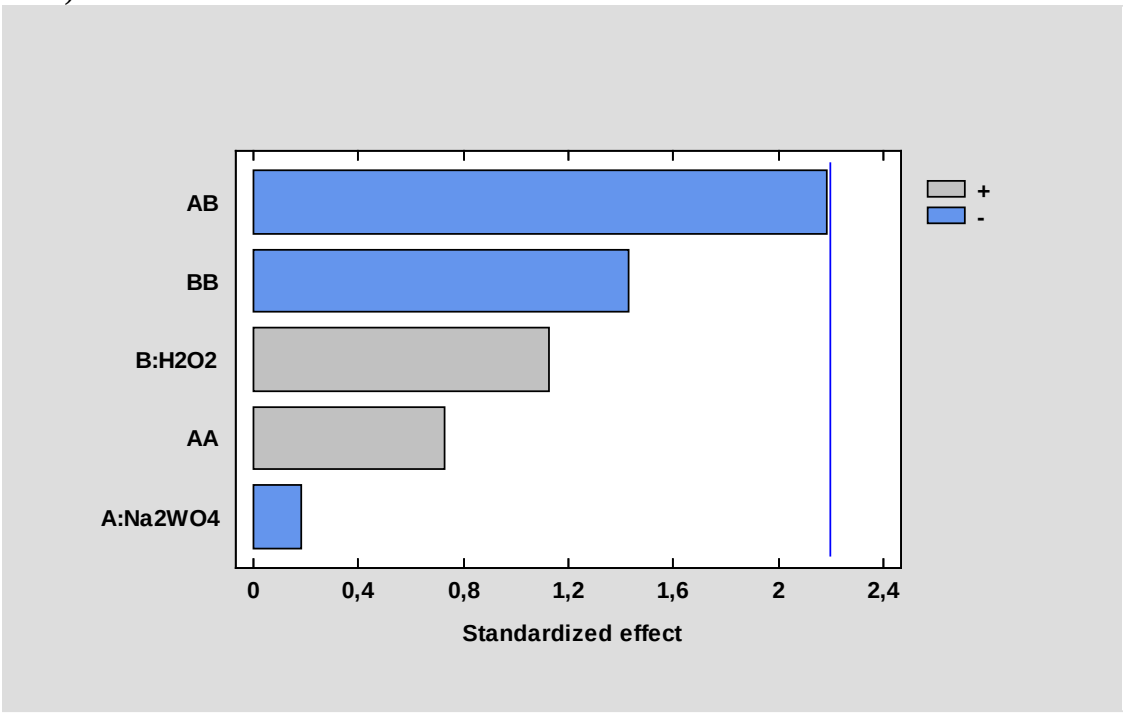


b) Pareto chart excluding AA effect

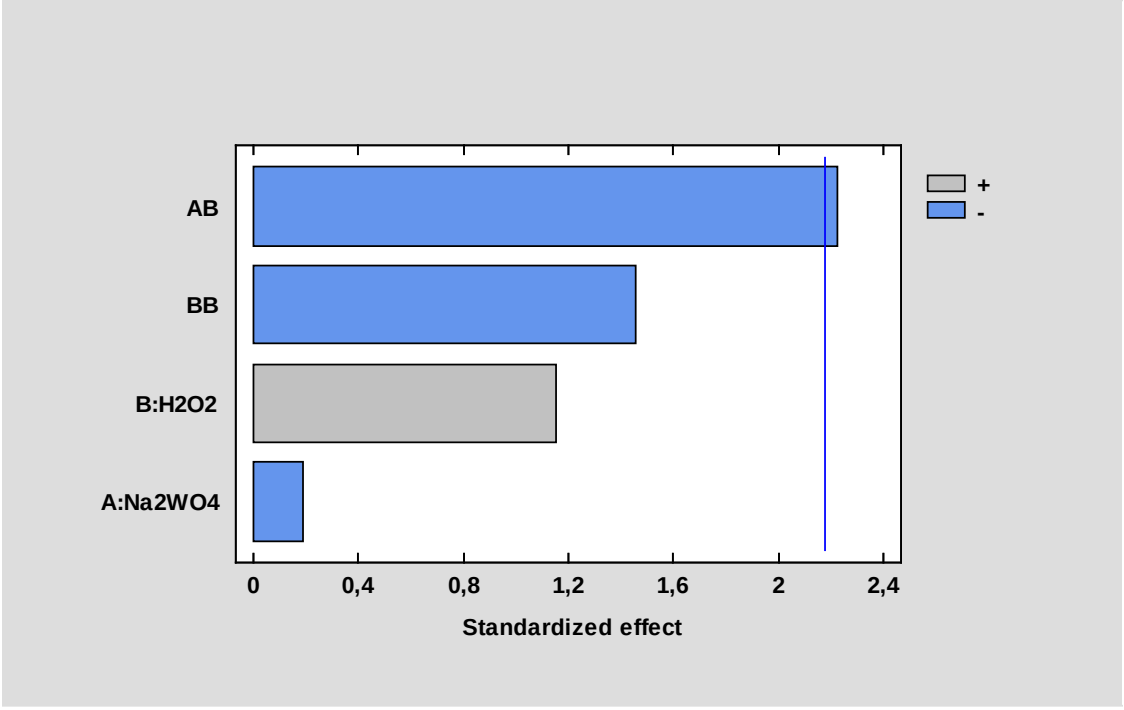


**Figure 13.** Pareto chart. Influence of the different parameters and their interactions a) and Pareto chart excluding the quadratic effect of $Na_2WO_4$.

**Table 1**. Weight percentages of the elements detected in the EDX spectra for the samples electrodeposited in 5mM $Na_2WO_4$ and 20 and 40 mM $H_2O_2$.

| Sample | | Ti (wt%) | W (wt%) | O (wt%) |
|---|---|---|---|---|
| **5mM $Na_2WO_4$ - 20mM $H_2O_2$** | Spectrum 1 | 9.04 | 86.35 | 4.61 |
| | Spectrum 2 | 62.42 | 3.01 | 34.57 |
| **5mM $Na_2WO_4$ - 40mM $H_2O_2$** | Spectrum 3 | 57.72 | 1.60 | 40.68 |
| | Spectrum 4 | 62.94 | 1.47 | 35.59 |
| | Spectrum 5 | 54.93 | 1.87 | 43.20 |

**Table 2**. Analysis of variance for the photocurrent density taking into account the factors $Na_2WO_4$ concentration, $H_2O_2$ concentration, the quadratic individual effects and the interaction between factors.

| | **Sum of Squares** | **Gl** | **Mean Square** | $F_{ratio}$ | ***p*-value** |
|---|---|---|---|---|---|
| $Na_2WO_4$ | 0,00000208333 | 1 | 0,00000208333 | 0,03 | 0,8584 |
| $H_2O_2$ | 0,0000795675 | 1 | 0,0000795675 | 1,27 | 0,2831 |
| $Na_2WO_4^2$ | 0,0000332544 | 1 | 0,0000332544 | 0,53 | 0,4809 |
| $Na_2WO_4 \cdot H_2O_2$ | 0,00029768 | 1 | 0,00029768 | 4,76 | 0,0516 |
| $H_2O_2^2$ | 0,000127314 | 1 | 0,000127314 | 7,36 | 0,1812 |
| Residual error | 0,00068721 | 11 | 0,0000624736 | | |
| Total | 0,00168716 | 17 | | | |

**Table 3**. Analysis of variance for the photocurrent density taking into account the factors $Na_2WO_4$ concentration, $H_2O_2$ concentration, the quadratic individual effect of $H_2O_2$ and the interaction between factors.

| | **Sum of Squares** | **Gl** | **Mean Square** | $F_{ratio}$ | ***p*-value** |
|---|---|---|---|---|---|
| $Na_2WO_4$ | 0,00000208333 | 1 | 0,00000208333 | 0,03 | 0,8553 |
| $H_2O_2$ | 0,0000795675 | 1 | 0,0000795675 | 1,33 | 0,2721 |
| $Na_2WO_4 \cdot H_2O_2$ | 0,00029768 | 1 | 0,00029768 | 4,96 | **0,0459** |
| $H_2O_2^2$ | 0,000127314 | 1 | 0,000127314 | 2,12 | 0,1710 |
| Residual error | 0,000720464 | 11 | 0,0000600387 | | |
| Total | 0,00168716 | 17 | | | |

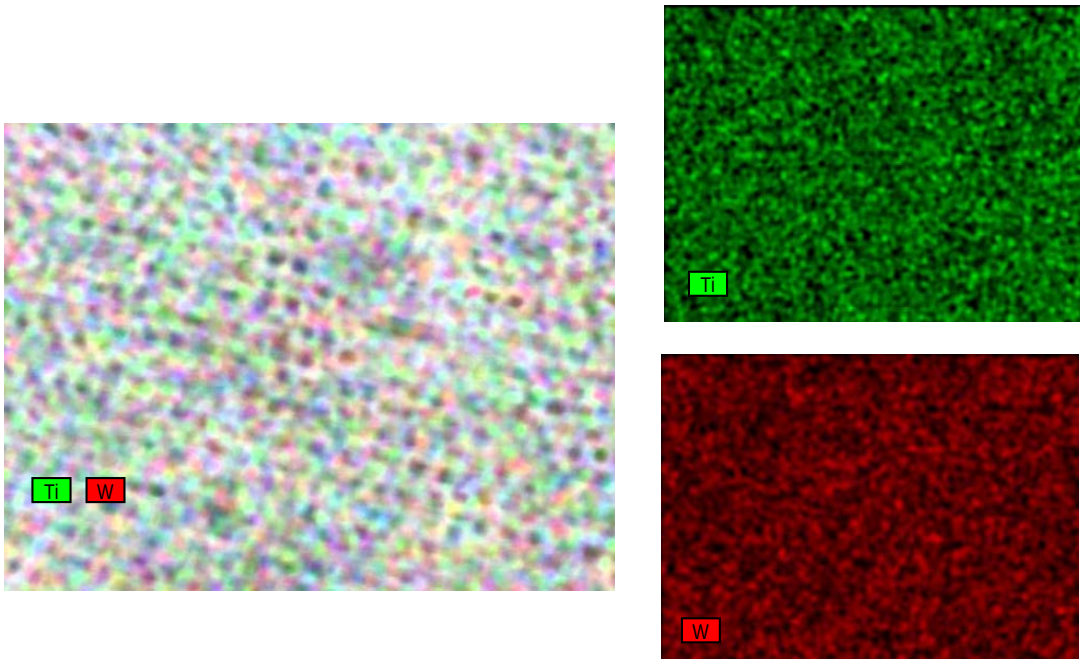


**Fig. S1.** EDX Mapping of the $TiO_2$-$WO_3$ nanostructures electrodeposited 25 mM $Na_2WO_4$ and 30 mM $H_2O_2$.

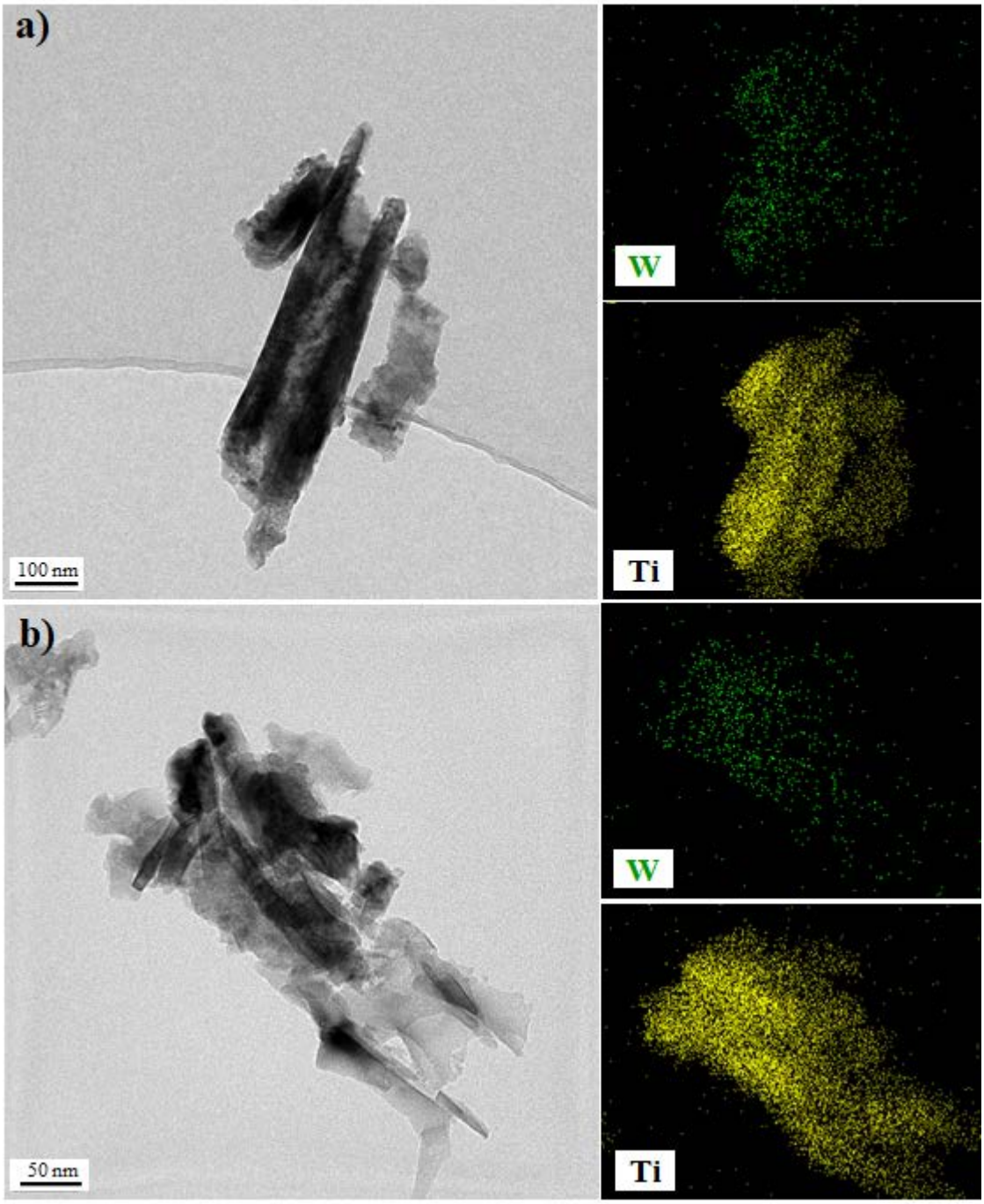


**Fig. S2.** HR-TEM images and EDX mapping of the $TiO_2$-$WO_3$ nanostructures electrodeposited at a) 5 mM $Na_2WO_4$ and 30 mM $H_2O_2$ and b) 15 mM $Na_2WO_4$ and 30 mM $H_2O_2$.

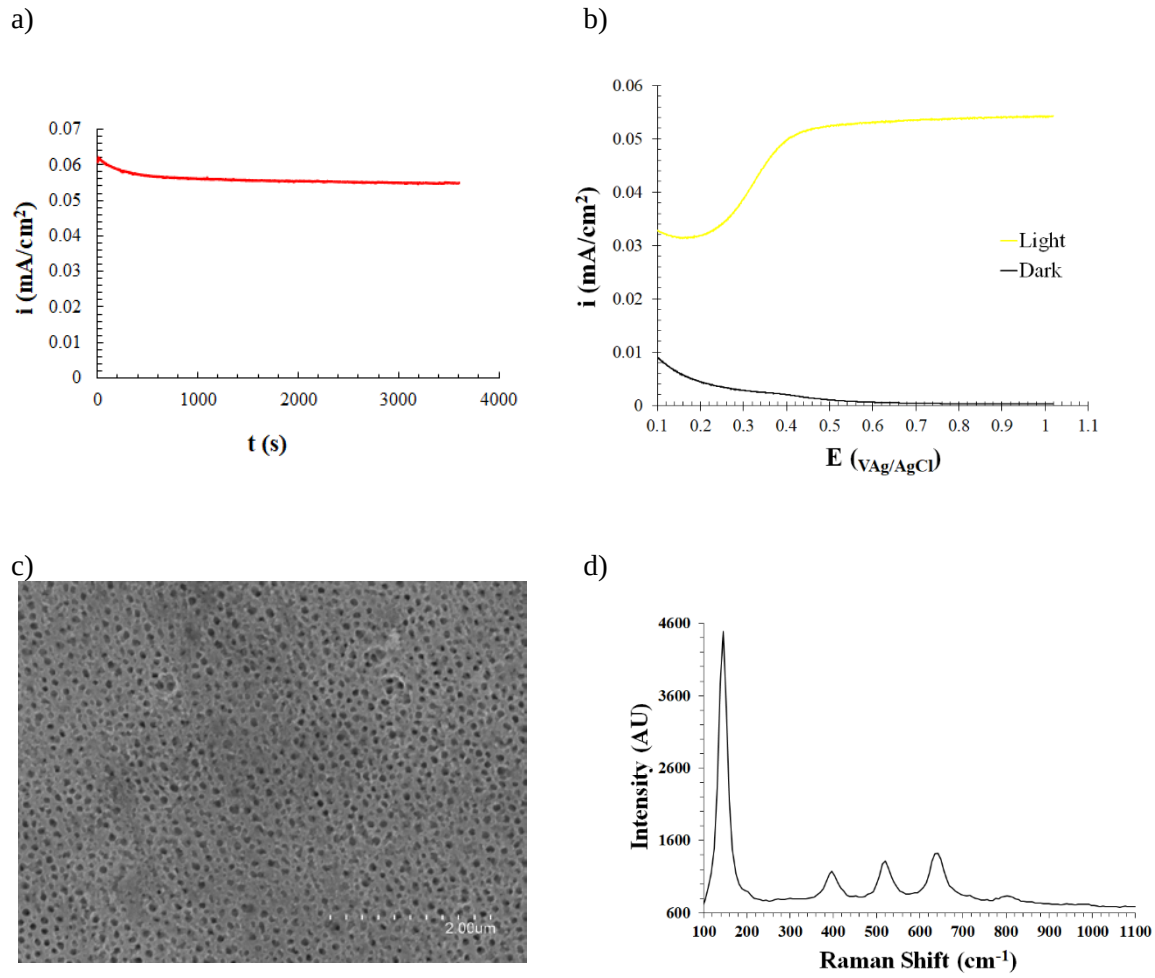


**Fig. S3.** Stability of the samples synthesized at 25 mM $Na_2WO_4$ and 30 mM $H_2O_2$ a) i-t curve (at $1V_{Ag/AgCl}$ under illumination), b) E-i curve (under illumination and dark conditions), FE-SEM image and Raman Spectra after stability tests c) and d), respectively.